NATIONAL BUREAU OF STANDARDS
MICROCOPY RESOLUTION TEST CHART

LEVEL

AN ANALYSIS OF THE DISK MICROSTRIP ANTENNA PART II

University of Illinois

Y. T. Lo
D. D. Harrison
W. F. Richards

D D C

JUL 3 1979

DDC FILE COPY

ROME AIR DEVELOPMENT CENTER
Air Force Systems Command
Griffiss Air Force Base, New York 13441

79 07 02 031

This report has been reviewed by the RADC Information Office (OI) and is releasable to the National Technical Information Service (NTIS). At NTIS it will be releasable to the general public, including foreign nations.

RADC-TR-79-132 has been reviewed and is approved for publication.

APPROVED: *John A. Strom*

JOHN A. STROM
Contract Monitor

APPROVED: *Allan C. Schell*

ALLAN C. SCHELL
Chief, Electromagnetic Sciences Division

FOR THE COMMANDER: *John P. Huss*

JOHN P. HUSS
Acting Chief, Plans Office

REPORT DOCUMENTATION PAGE		READ INSTRUCTIONS BEFORE COMPLETING FORM
1. REPORT NUMBER RADC-TR-79-132-PT-2	2. GOVT ACCESSION NO.	3. RECIPIENT'S CATALOG NUMBER
4. TITLE (and Subtitle) AN ANALYSIS OF THE DISK MICROSTRIP ANTENNA. PART II.		5. TYPE OF REPORT & PERIOD COVERED Interim Report #2 no. 2
		6. PERFORMING ORG. REPORT NUMBER EM-78-19, UILU-ENG-78-2564
7. AUTHOR(s) Y. T. Lo D. D. Harrison W. F. Richards		8. CONTRACT OR GRANT NUMBER(s) F19682-78-C-0025
9. PERFORMING ORGANIZATION NAME AND ADDRESS University of Illinois at Urbana-Champaign Dept of Electrical Engineering/Electromagnetics Lab Urbana IL 61801		10. PROGRAM ELEMENT, PROJECT, TASK AREA & WORK UNIT NUMBERS 61102F 2305J323 J3
11. CONTROLLING OFFICE NAME AND ADDRESS Deputy for Electronic Technology (RADC/EEA) Hanscom AFB MA 01731		12. REPORT DATE May 1979
		13. NUMBER OF PAGES 91
14. MONITORING AGENCY NAME & ADDRESS(if different from Controlling Office) Same		15. SECURITY CLASS. (of this report) UNCLASSIFIED
		15a. DECLASSIFICATION DOWNGRADING SCHEDULE N/A

16. DISTRIBUTION STATEMENT (of this Report)

Approved for public release; distribution unlimited.

UIEM-78-19-PT-2, UILU-ENG-78-2564-PT-2

17. DISTRIBUTION STATEMENT (of the abstract entered in Block 20, if different from Report)

Same

18. SUPPLEMENTARY NOTES

RADC Project Engineers: John A. Strom and Nicholas Kernweis (EEA)

19. KEY WORDS (Continue on reverse side if necessary and identify by block number)

Disk Microstrip Antennas
Excitation of cavity and input Impedance
Multi-port disk microstrip antennas

20. ABSTRACT (Continue on reverse side if necessary and identify by block number)

Disk microstrip antennas are treated as cavities, from which both internal and external (radiation) field can be determined, based on an efficient improved theory. This theory can predict the impedance characteristics very accurately even for cases where the dominant mode is not strongly excited. The theory is extended to two-port disk microstrip antennas. In particular, if one port is shorted the input resonant impedance at another port on the circumference can be varied over orders of magnitude by simply changing the relative angular

DD FORM 1473
1 JAN 73

positions between the two ports. In case of a single port a similar
variation of input impedance can be achieved by moving the feed in
the radial direction. All of these provide a means for impedance
matching with practically no effect on the pattern. So far as the
input impedance matching is concerned the antenna can be represented
accurately by a parallel resonant circuit in series with an inductance.
The former derives from the resonant·mode term and the latter from all
non-resonant terms of the field solution in expansion. Experiments
have been conducted to verify the theoretical results. Excellent
agreement is observed in all cases.

Accession For

NTIS GRA&I	☑
DDC TAB	☐
Unannounced	☐
Justification	

By

Distribution/

Availability Codes

Dist	Avail and/or special
A	

TABLE OF CONTENTS

i

INTRODUCTION

1.1 Motivation for the Use of Microstrip Antennas

In recent years there has been an increased interest in microstrip antennas, primarily due to their surface conformability, compact structure and ease of construction. A general microstrip antenna can be pictured as in Figure 1.1. The antenna element is separated from the ground plane by a suitable low-loss dielectric medium. Since these antennas have such a low profile, they are suitable for high velocity vehicles where wind drag must be kept to a minimum.

Experimentally, these antennas have been found to have a relatively narrow bandwidth. Yet because these antennas are so thin, there is still active interest in finding a simple analytic model to describe and predict their behavior.

A major use for the microstrip antenna is as an element in an array. Experimental results indicate that no "magic" element shape exists that will give a substantially wider impedance bandwidth than any other shape. For this reason, it would seem more important to concentrate on a short list of simple geometries, rather than a long list of random geometries. Of course, the short list must include elements whose radiation patterns are sufficiently varied, so as to allow a broad range of array design. Such a list could include the disk, half disk, annulus, rectangle, square and triangle. A simple and accurate theory has been developed for use with these geometries. In Chapter 2, the
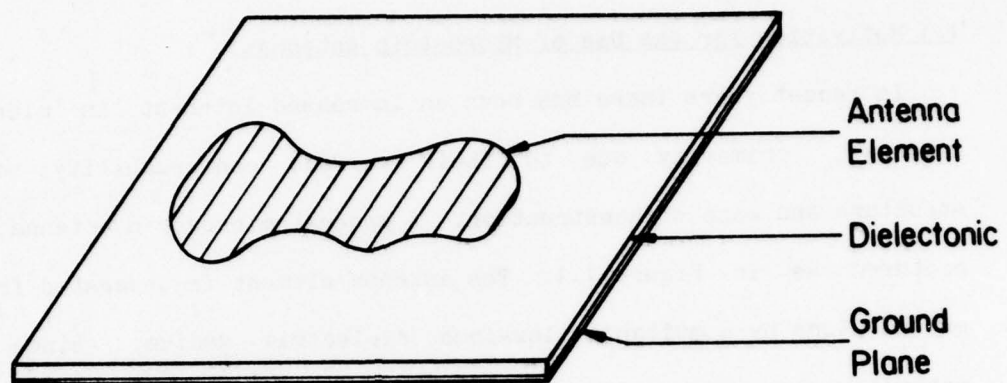
1

Figure 1.1.   A general microstrip antenna element.

disk element is analyzed, and the method of analysis can also be applied
to other simple geometries.

1.2 Literature Review

In the literature, some scattered and limited attempts have been
made to analyze the behavior of a few microstrip elements. Some of
these attempts have incorporated doubtful and even invalid assumptions.

Munson's analysis of the rectangular element is one example, [1].
It was claimed that the input impedance could be modelled as two slot
antennas separated by a low impedance transmission line. The obvious
oversight is that this uses superposition of the power patterns of the
two slots, thus neglecting any mutual coupling. A similar approach was
used by Derneryd [2]. No attempt was made to compare calculated and
measured input impedance results in either [1] or [2], and their
analysis is very limited since the feed point must remain on that edge
of the rectangle where the E field is constant. Finally, the method can
not be used for any other element shape.

Another method [3] used a grid of linear and V shaped dipoles to
approximate the radiating element. This method shows an agreement
between calculated and measured input impedances that is quite inferior
to that obtained by the simple analysis in Chapter 2. Even so, the
method was inefficient with respect to the computer time required. The
analysis of Chapter 2 shows excellent results, and requires orders of
magnitude less computer time than that of [3]. As an example, the
resonant radiation pattern and the input impedance for 15 frequencies
near resonance were calculated in under 2 seconds for a disk antenna.

CHAPTER 2

ANALYSIS OF THE MICROSTRIP DISK

2.1 The Simple Cavity Model

The method used in analyzing the disk is somewhat different from methods found in the literature, and is quite simple. Analytic results obtained using this method agree very well with measured data, and it appears that validity has not been sacrificed for simplicity.

Power is fed to the antenna by either a coaxial line piercing the ground plane, or by a microstrip transmission line at the edge, as shown in Figure 2.1. The antenna is modelled as a closed cavity, bounded on top and bottom by perfect electric conducting (PEC) planes, and around the perimeter by a perfect magnetic conducting (PMC) ribbon as in Figure 2.2. Henceforth, the disk will be oriented with the z axis as shown.

The PMC wall approximation would seem plausible with respect to the fields between the conducting planes since the radially directed surface current (on the underside of the top PEC plane) must approach zero at the edge. Of course, this can not be assumed for the external fields since such a boundary would not allow radiation. However, the radiated power can be approximated once the internal fields are known at the edge. The source of the radiation is taken to be the edge distribution of the internal fields. Calculating the radiated power in this manner requires the assumption that the internal field structure is relatively independent of the radiated power. The measured quality factor of these microstrip antennas is high so that this assumption is plausible.
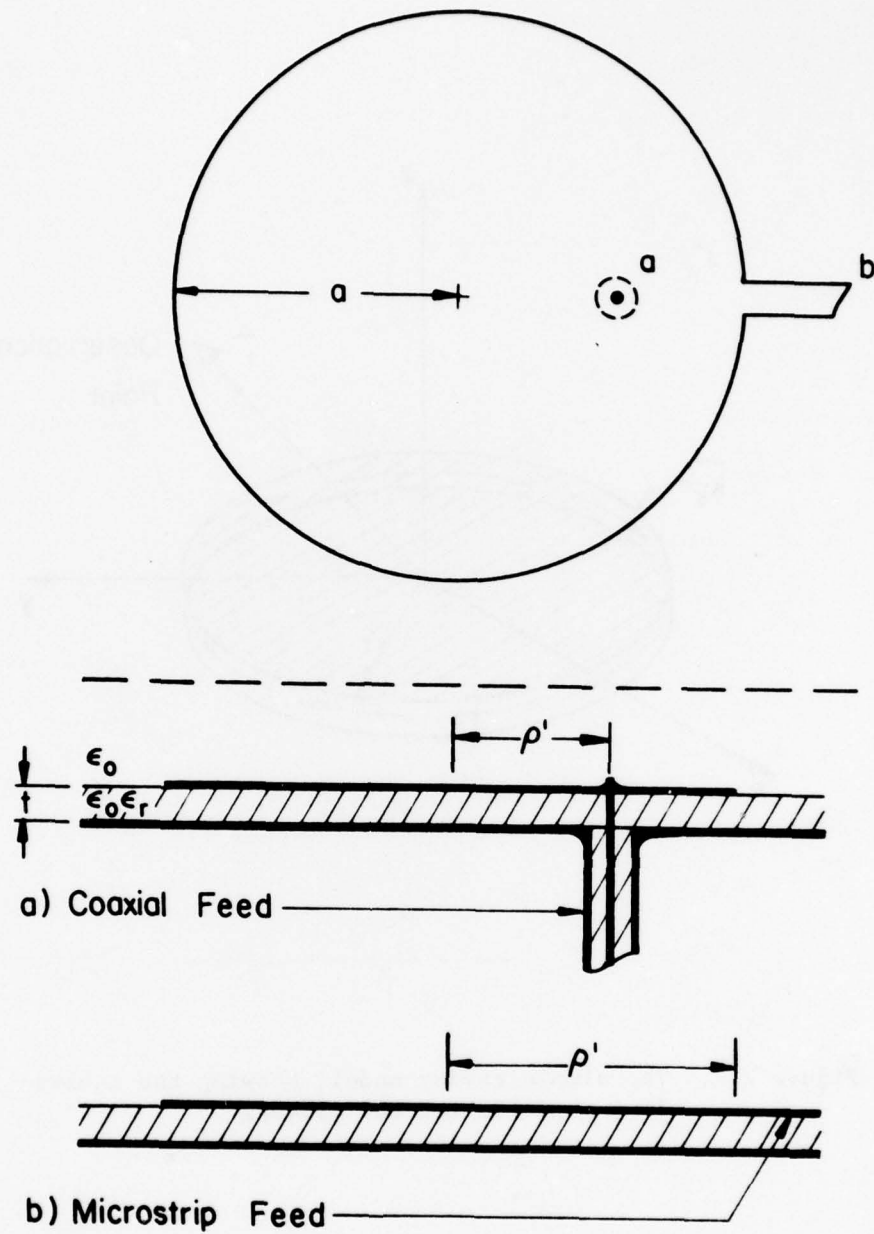
Figure 2.1.   A disk element, showing coaxial and microstrip
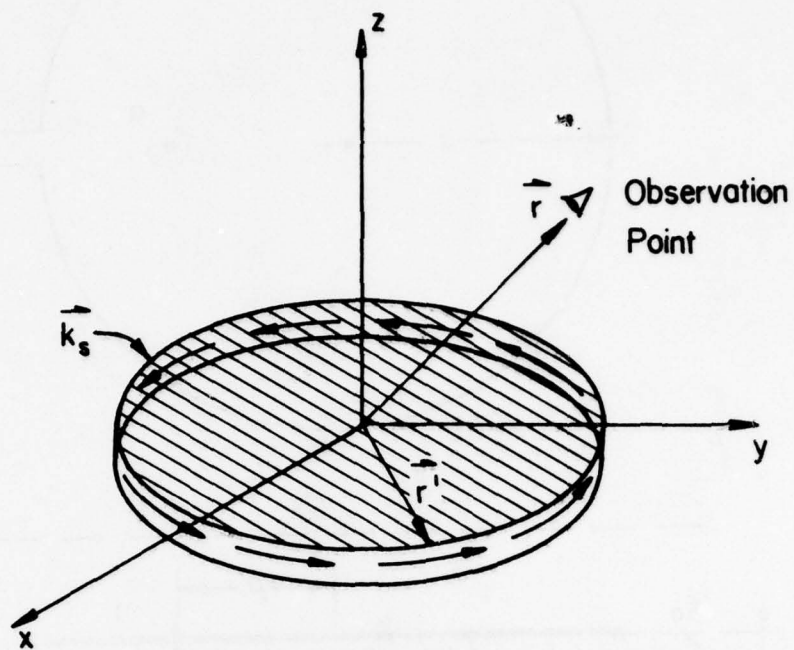feed methods.

Figure 2.2. The simple cavity model, showing the equivalent magnetic current ribbon.

Since the antenna is relatively thin, the internal fields are taken to be TEM. Indeed, for the frequencies of interest, the TE and TM modes of all orders are well below cutoff and the electric field is perpendicular to the disk surface, with no divergence.

When excited, the internal field structure of this simple cavity model can be found using either mode matching or a modal expansion. It is then straightforward to calculate the stored energy, radiated power, internal copper loss and the driving point voltage. When all of these parameters have been determined, the input impedance and radiation pattern can be computed. It is because the geometries are simple and fit nicely into some coordinate system that mode matching and modal expansion can be used here. This is one motivating factor for concentrating on a short list of simple element shapes.

2.2 The Internal Field Structure

As mentioned, the internal fields can be found using either mode matching or a modal expansion. Since the numerical results are found using a computer, it is advantageous to investigate both methods for simplicity and/or speed of calculation.

Within the cavity the fields must satisfy the boundary conditions and the vector wave equation. However, one major difference between modal expansion and mode matching is in the way the individual mode terms satisfy these conditions. Although both methods use an infinite set of orthogonal functions (modes), a resonant mode expansion requires that each mode term satisfies the boundary conditions, and that the

7

total field satisfies the inhomogeneous wave equation. Mode matching requires that the sum satisfies the source condition, and that each term obeys the source free wave equation.

The vector wave equation is well known to be

$$\nabla^2 \vec{E} + K_1^2 \vec{E} = j\omega\mu\vec{J} - \frac{\nabla(\nabla \cdot \vec{J})}{j\omega\epsilon} \quad , \qquad (2.2.1)$$

where K_1 is the complex wave number in the dielectric. For the thin cavity, the source $\vec{J}$ has some special properties. For the microstrip feed, the source current is assumed to be just $\hat{n}$ X $\vec{H}$, where H is the TEM H field of the transmission line. For the coaxial feed, the source is taken to be equal to the current density on the center conductor, as it existed in the coax. However, this source is simplified by considering the current distribution to lie on a cylinder of constant radius. Thus both sources are considered as rectangular distributions in ϕ and as having no divergence. For simplicity the total feed current is assumed to be one ampere, flowing into the port. Both source distributions are of the form shown in Figure 2.3. Therefore, Equation (2.2.1) reduces to

$$\nabla^2 E_z + K_1^2 E_z = j\omega\mu J_z \quad . \qquad (2.2.2)$$

It should be mentioned that for a coaxial feed, no attempt has been made to enforce the boundary condition that E_z must be zero on the coaxial center conductor. Yet, from the good agreement obtained between the calculated and measured results of Chapter 3, this appears to be of
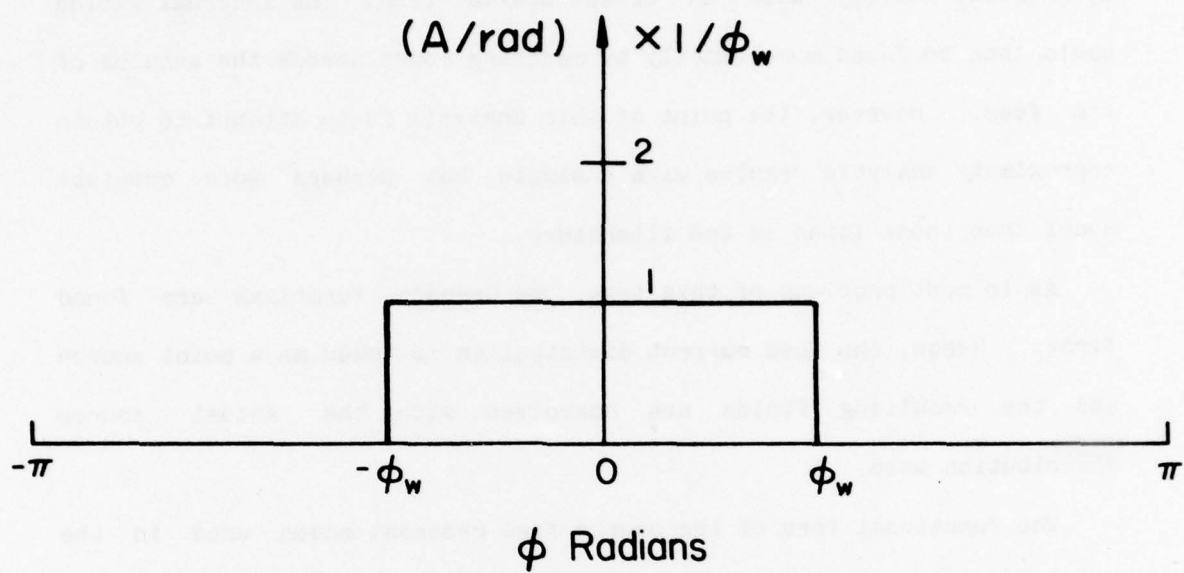
8

Figure 2.3. The source current distribution used to model
the coaxial and microstrip feeds.

no major consequence. This could be attributed to the fact that the conductor length, within the antenna, is very short.

A more rigorous treatment might be to consider the system as a cylindrical cavity with an offset coaxial feed. The internal fields could then be found more exactly by matching modes across the annulus of the feed. However, the point of this analysis is to attempt to obtain approximate analytic results with a simple but perhaps more complete model than those found in the literature.

As in most problems of this type, the Green's functions are found first. Hence, the feed current distribution is taken as a point source and the resulting fields are convolved with the actual source distribution used.

The functional form of the source free resonant modes used in the modal expansion is found from

$$\nabla^2 \psi_{mn} + K_{mn}^2 \psi_{mn} = 0 . \tag{2.2.3}$$

In cylindrical coordinates this gives

$$\psi_{mn} = J_n(K_{mn}\rho)\cos(n\phi) . \tag{2.2.4}$$

In terms of these modes, the electric field can be expanded as follows:

$$E_z = \sum_{\substack{m,n \\ =0}}^{\infty} A_{mn} \psi_{mn} . \tag{2.2.5}$$

From Maxwell's equations the H field for each term is

10

$$H_{mn} = \frac{j}{\omega\mu} \left[\frac{\partial\Psi_{mn}}{\rho\partial\phi} \hat{\rho} - \frac{\partial\Psi_{mn}}{\partial\rho} \hat{\phi} \right] A_{mn} \ . \tag{2.2.6}$$

Since the exterior boundary condition is that $H_{\phi mn} = 0$,

$$J_n'(K_{mn}a) = 0 \ , \tag{2.2.7}$$

where a is the disk radius. Therefore, the resonant frequencies are those where $(K_{mn}a)$ is a zero of J_n.

Requiring the total field to satisfy the inhomogeneous wave equation gives

$$j\omega\mu I\delta(\phi)\delta(\rho - \rho')/\rho' = \sum_{\substack{m,n \\ =0}}^{\infty} A_{mn}(K_1^2 - K_{mn}^2)\Psi_{mn} \ , \tag{2.2.8}$$

where

$$\nabla^2\Psi_{mn} = -K_{mn}^2\Psi_{mn} \ , \tag{2.2.9}$$

from Equation (2.2.3). Here, I is the source current in amperes and, from the symmetry of the disk, the source is taken to be at $(\rho',\phi = 0)$. The fact that the $\{\Psi_{mn}\}$ are orthogonal can be used as an advantage. Indeed if

$$C_1 K_{mn} J_n'(K_{mn}a) + C_2 J_n(K_{mn}a) = 0 \ , \tag{2.2.10}$$

then from

11

$$\int_0^a J_n(K_{mn}\rho)J_q(K_{pq}\rho)\rho d\rho =$$

$$\begin{cases} \dfrac{a^2}{2}\left\{\left[J_n{}'(K_{mn}a)\right]^2 + \left[J_n(K_{mn}a)\right]^2\left[1 - \dfrac{n^2}{(K_{mn}a)^2}\right]\right\}, & (m,n)=(p,q) \\ 0, & \text{otherwise}. \end{cases} \qquad (2.2.11)$$

we can say

$$j\omega\mu I \int_\rho \int_\phi \frac{\delta(\phi')\delta(\rho\ \rho')}{\rho}\Psi_{pq}\rho d\rho d\phi = \tag{2.2.12}$$

$$\sum_{m,n} A_{mn}(K_1^2 - K_{mn}^2)\int_\rho\int_\phi \Psi_{mn}\Psi_{pq}\rho d\rho d\phi .$$

Performing the integrals gives

$$A_{mn} = \frac{2j\omega\mu J_n(K_{mn}\rho')}{\pi a^2(1 + \delta_{m0})J_n{}^2(K_{mn}a)(K_1^2 - K_{mn}^2)\left\{1 - \dfrac{n^2}{(K_{mn}a)^2}\right\}} . \tag{2.2.13}$$

Finally, from Equation (2.2.4)

$$E_z = \sum_{\substack{m,n \\ =0}}^\infty A_{mn}J_n(K_{mn}\rho)\cos(n\phi) . \tag{2.2.14}$$

For the mode matching case, one needs to consider the homogeneous equation in each source-free region. This is

12

$$\nabla^2 \Psi_m + K_1^2 \Psi_m = 0 \tag{2.2.15}$$

where

$$\Psi_m = J_m(K_1 \rho)\cos(m\phi) \qquad \text{or} \qquad \Psi_m = Y_m(K_1 \rho)\cos(m\phi) \tag{2.2.16}$$

or any linear combination of Y_m and J_m. The source

$$\vec{J} = If(\phi)\delta(\rho - \rho')/\rho' \tag{2.2.17}$$

can be restated in terms of its Fourier components. Hence,

$$\vec{J} = \frac{I\delta(\rho - \rho')}{\pi\rho'} \sum_{m=0}^{\infty} W_m \frac{\cos(m\phi)}{(1 + \delta_{mo})} \tag{2.2.18}$$

Therefore, the source current can be considered to be a sum of cylindrical current sheets located at $\rho = \rho'$.

For the Green's functions, $f(\phi)$ is the Dirac delta. Figure 2.4 shows the two regions of the disk, separated by the cylindrical current sheets. Matching of the fields across these current sheets constitutes the source condition.

In region 1, $\rho' < \rho < a$, and

$$E_{z_1} = \sum_{m=0}^{\infty} \{ A_m J_m(K_1 \rho) + B_m Y_m(K_1 \rho) \} \cos(m\phi) \tag{2.2.19}$$
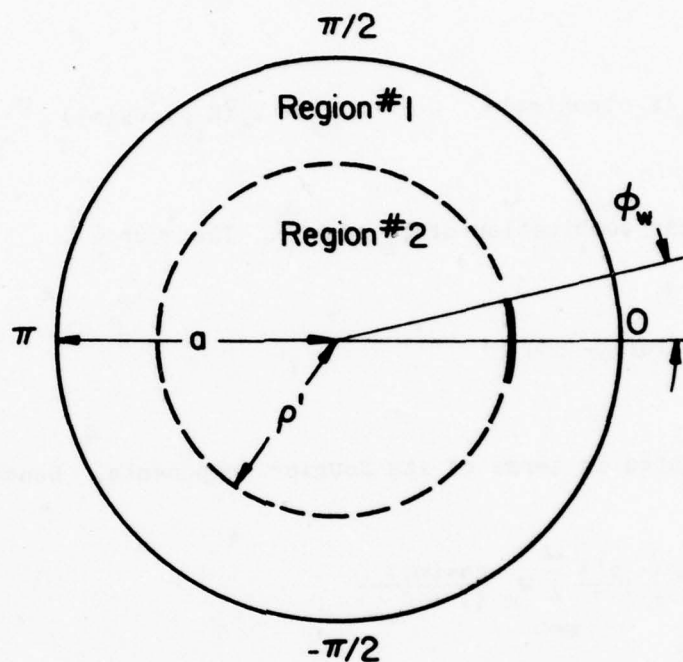
At $\rho = a$,

Figure 2.4. The disk, showing a source current distribution, the location of the equivalent cylindrical current sheets, and the two source free regions of the mode-matching analysis.

$$\frac{\partial E_{z_1}}{\partial \rho} = 0 \tag{2.2.20}$$

With the orthogonality of the $\cos(m\phi)$, the result from region 1 is

$$\{A_m J_m{}'(K_1 a) + B_m Y_m{}'(K_1 a)\} = 0 \ . \tag{2.2.21}$$

where the derivative is with respect to the entire argument.

In region 2, Bessel functions of the second kind are not permissible since they require a singularity at $\rho = 0$. Hence,

$$E_{z_2} = \sum_{m=0}^{\infty} C_m J_m(K_1 \rho) \cos(m\phi) \tag{2.2.22}$$

Using Equations (2.2.19) and (2.2.22) and requiring E_z to be continuous at the source gives

$$A_m J_m(K_1 \rho') + B_m Y_m(K_1 \rho') = C_m J_m(K_1 \rho') \tag{2.2.23}$$

where the orthogonality of $\cos (m\phi)$ has been used.

At the source

$$\hat{\rho} \ X \ (H_1 - H_2)\hat{\phi} = \vec{J} \tag{2.2.24}$$

From Equation (2.2.6) and orthogonality,

15

$$\frac{jK_1}{\omega\mu} \left[(C_m - A_m) J_m'(K_1\rho') - B_m Y_m'(K_1\rho') \right] = \frac{1}{\pi\rho'(1 + \delta_{mo})} \cdot \quad (2.2.25)$$

Equations (2.2.21), (2.2.23) and (2.2.25) constitute a determined set of equations for the A_m, B_m and C_m. Using Cramer's rule for determinants yields

$$A_m = - \frac{j\omega\mu Y_m'(K_1 a) J_m(K_1\rho')}{2(1 + \delta_{mo}) J_m'(K_1 a)} \quad , \qquad B_m = \frac{j\omega\mu J_m(K_1\rho')}{2(1 + \delta_{mo})} \quad ,$$

$$(2.2.26)$$

$$C_m = - \frac{j\omega\mu \{ J_m(K_1\rho') Y_m'(K_1 a) - Y_m(K_1\rho') J_m'(K_1 a) \}}{2(1 + \delta_{mo}) J_m'(K_1 a)} \cdot$$

Finally, Equations (2.2.19) and (2.2.22) can be used to find the electric field anywhere in the disk, due to a point source.

The results from the resonant mode expansion and from mode matching can be checked for consistency by comparing the E field Green's functions from the two methods. From the theory of complex variables, two systems are equal if their residues are equal and neither system has poles at infinity.

Consider any point within region 2 of Figure 2.4. Multiplying Equations (2.2.14) and (2.2.22) by $(K_1^2 - K_{mn}^2)$ and taking the limit as K_1 approaches K_{mn} gives

$$\frac{2j\omega\mu J_n(K_{mn}\rho')J_n(K_{mn}\rho)}{a^2\pi J_n^2(K_{mn}a)\left[1 - \frac{n^2}{(K_{mn}a)^2}\right]} \cdot \lim_{K_1 \to K_{mn}} \frac{(K_1^2 - K_{mn}^2)}{J_n'(K_{mn}a)}$$

$$\text{(2.2.27)}$$

$$= -\frac{j\omega\mu}{2} J_n(K_{mn}\rho)J_n(K_{mn}\rho')Y_n'(K_{mn}a) .$$

But since

$$\lim_{K_1 \to K_{mn}} \frac{(K_1^2 - K_{mn}^2)}{J_n'(K_{mn}a)} = \frac{2K_{mn}}{aJ_n''(K_{mn}a)} , \qquad \text{(2.2.28)}$$

the relationship simplifies to

$$\frac{2}{\pi(K_{mn}a)} = \frac{Y_n'(K_{mn}a)J_n^2(K_{mn}a)}{J_n'(K_{mn}a)}\left[1 - \frac{n^2}{(K_{mn}a)^2}\right] . \qquad \text{(2.2.29)}$$

The Wronskian relation that

$$\frac{2}{\pi(K_{mn}a)} = Y_n'(K_{mn}a)J_n(K_{mn}a) - J_n'(K_{mn}a)Y_n(K_{mn}a) , \qquad \text{(2.2.30)}$$

gives the requirement that

$$J_n''(K_{mn}a) = J_n(K_{mn}a)\left[1 - \frac{n^2}{(K_{mn}a)}\right] \qquad \text{(2.2.31)}$$

for the two methods to be consistent. But, Equation (2.2.31) is true from Bessel's differential equation, and inspection of Equations (2.2.14) and (2.2.22) shows that no poles lie at $K_{mn} = \infty$. Similar results can be shown for any point in region 1 of Figure 2.4. Thus, mode matching and a resonant mode expansion yield identical results for

17

the simple cavity model where the divergence of the source is zero.

Equations (2.2.14) and (2.2.22) indicate that evaluation of the internal fields requires a double summation for a modal expansion and a single summation for mode matching. Hence, it appears that less computational effort is required when using the results from mode matching.

The fields due to a source with a specific feed width are found by convolving the Green's functions with the source distribution. Thus,

$$E_z = \frac{P_a(\phi)}{2a} \star \sum_{m=0}^{\infty} F_m(\rho) \cos(m\phi)$$

$$(2.2.32)$$

$$= \sum_{m=0}^{\infty} F_m(\rho)\cos(m\phi) \frac{\sin(ma)}{(ma)} .$$

Here $P_a(\phi)$ is the unit "pulse" of width $2a$, and $F_m(\phi)$ is the separated ρ-dependent function found in equations (2.2.19) and (2.2.22). Therefore, the electric and magnetic fields are simply the Green's functions multiplied by $\{\sin(ma)\}/(ma)$. In regions 1 and 2 the electric fields are then

$$E_{z1} = \sum_{m=0}^{\infty} \{A_m J_m(K_1\rho) + B_m Y_m(K_1\rho)\} \cos(m\phi) \frac{\sin(m\phi_w)}{m\phi_w} ,$$

$$(2.2.33)$$

$$E_{z2} = \sum_{m=0}^{\infty} C_m J_m(K_1\rho) \cos(m\phi) \frac{\sin(m\phi_w)}{m\phi_w} .$$

18

2.3 Dissipation, Radiation, and the Stored Energy

With the E field known throughout the disk, the time-averaged electric stored energy can be found from

$$W_e = \frac{\varepsilon}{2} \int_V |E|^2 \, dv \ . \tag{2.3.1}$$

The forms for the fields in regions 1 and 2 of Figure 2.4 are stated in Equation (2.2.33). Since the fields are separable in ϕ, θ and z, the volume integrals are easy to evaluate.

Let the electric field be represented in the following manner:

$$E_{z_1} = \frac{-j\omega\mu}{2} \sum_{m=0}^{\infty} P_m(\rho)\cos(m\phi),$$

$$\tag{2.3.2}$$

$$E_{z2} = \frac{-j\omega\mu}{2} \sum_{m=0}^{\infty} Q_m(\rho)\cos(m\phi) \ .$$

Then, the electric stored energy is expressible as

$$W_e = \frac{\varepsilon_o \varepsilon_r (\omega\mu)^2 t}{8} \sum_{m=0}^{\infty} \sum_{n=0}^{\infty} \left\{ \left[\int_0^{\rho'} Q_m Q_n^{*}\rho d\rho + \int_{\rho'}^{a} P_m P_n^{*}\rho d\rho \right] \right.$$

$$\tag{2.3.3}$$

$$\left. \cdot \int_0^{2\pi} \cos(m\phi)\cos(n\phi)d\phi \right\} \ .$$

Since the last integral is zero except when $m = n$,

$$W_e = \frac{\varepsilon_o \varepsilon_r (\omega\mu)^2 t\pi}{8} \sum_{m=0}^{\infty} \left[\int_0^{\rho'} |Q_m|^2\rho d\rho + \int_{\rho'}^{a} |P_m|^2\rho d\rho \right] \ . \tag{2.3.4}$$

Each integral in this equation can be evaluated in closed form since the

19

P_m and Q_m are just

$$P_m = \{A_m J_m(K_1\rho) + B_m Y_m(K_1\rho)\} \, \frac{\sin(m\phi_w)}{m\phi_w} \, ,$$

$$Q_m = C_m J_m(K_1\rho) \, \frac{\sin(m\phi_w)}{(1 + \delta_{m0})m\phi_w} \, . \tag{2.3.5}$$

where A_m, B_m and C_m are given by Equation (2.2.26). It is well known that

$$\int_a^b U_m^2(K_1\rho)\rho d\rho = \frac{\rho^2}{2} \left\{ \left[U_m{}'(K_1\rho) \right]^2 \right.$$

$$\left. + \left[1 - \frac{n^2}{(K_1\rho)^2} \right] \left[U_m^2(K_1\rho) \right] \right\} \Big|_a^b \, , \tag{2.3.6}$$

where U_m is any linear combination of J_m and Y_m. By taking the summation inside the integrals of Equation (2.3.4), the electric stored energy can also be evaluated using a numerical quadrature. Thus,

$$W_e = \frac{\epsilon_0 \epsilon_r \pi t (\omega\mu)^2}{8} \left[\int_0^{\rho'} \sum_{m=0}^{\infty} |Q_m|^2 (1 + \delta_{mo})\rho d\rho \right.$$

$$\left. + \int_{\rho'}^a \sum_{m=0}^{\infty} |P_m|^2 (1 + \delta_{mo})\rho d\rho \right] \, . \tag{2.3.7}$$

The power dissipated in the dielectric can be found from

$$P_d = \sigma \int_v |E|^2 dv \, . \tag{2.3.8}$$

But this is just

$$P_d = 2\omega\delta W_e \, , \tag{2.3.9}$$

where δ is the dielectric loss tangent.

20

The copper loss is approximated by initially assuming that it does not change the internal field structure. Therefore it is calculated using the internal fields derived with perfectly conducting boundaries. Again, this method is plausible since the copper loss is very small with respect to the reactive power within the disk. The copper loss is related to the H field tangent to, and the E field normal to the copper boundary.

In a good conductor the skin depth is

$$\Delta = \sqrt{\frac{2}{\omega\mu\sigma}} \, , \tag{2.3.10}$$

where σ is the conductivity in mho-cm. For the loss due to the tangential H field, the current density (J_v) within the copper is assumed such that

$$\int_0^\infty J_v dz = J_s \, , \tag{2.3.11}$$

where J_s is the surface current density that would exist if the conductivity were infinite. J_v is the unknown volume current density flowing parallel to the surface, with form

$$|J_v| = |J_o| e^{-z/\Delta} \, . \tag{2.3.12}$$

Therefore,

21

$$|J_0| = J_s/\Lambda \qquad\qquad\qquad (2.3.13)$$

so that

$$|J_v| = \frac{|J_s|e^{-z/\Lambda}}{\Lambda} \quad . \qquad\qquad\qquad (2.3.14)$$

Since the fields are assumed to be TEM,

$$|J_s| = |H| \quad . \qquad\qquad\qquad (2.3.15)$$

The power dissipated in the copper is

$$P_{cu_1} = \frac{1}{\sigma} \int_v |J_v|^2 dv \qquad\qquad\qquad (2.3.16)$$

so that

$$P_{cu_1} = \frac{2}{\sigma\Lambda^2} \int_{z=0}^{\infty} e^{-2z/\Lambda} \int_{r=0}^{a} \int_{\phi=0}^{2\pi} |J_s|^2 \quad . \qquad\qquad (2.3.17)$$

But this is just

$$P_{cu_1} = \frac{2}{\sigma\Lambda t\mu} W_h \quad , \qquad\qquad\qquad (2.3.18)$$

where the factor 2 accounts for both top and bottom boundaries.

22

The copper loss due to the E field is found using the fact that the normal D field is continuous at the copper boundary. Since the permittivities of the dielectric and copper are

$$\epsilon_d = \epsilon_o \epsilon_r$$

$$\epsilon_{cu} = \epsilon_o \left[1 + \frac{\sigma}{j\omega\epsilon_o} \right] ,$$

(2.3.19)

and for a good conductor

$$\frac{\sigma}{j\omega\epsilon_o} \gg 1 ,$$

(2.3.20)

then

$$E_{cu} \doteq \frac{j\omega\epsilon_o \epsilon_r}{\sigma} E_d .$$

(2.3.21)

The general copper loss is

$$P_{cu} = \sigma \int_v |E|^2 dv .$$

(2.3.22)

Since the E field in the copper varies in the z direction as

$$|E_{z\ cu}| = e^{-z/\Delta} ,$$

(2.3.23)

the copper loss due to E_z is

$$P_{cu_2} = \frac{\Delta(\epsilon_o \epsilon_r \omega)^2}{\sigma} \int_{\phi=0}^{2\pi} \int_{\rho=0}^{a} |E_d|^2 ds .$$

(2.3.24)

23

where, again, the factor 2 accounts for both top and bottom boundaries. This is expressible as

$$P_{cu_2} = \frac{\Delta^2 K_1^{\,2} W_e}{\sigma t \mu \Delta} \cdot$$ (2.3.25)

The total power loss in the copper is now seen to be

$$P_{cu} = \frac{2W_h + \Delta^2 K_1^{\,2} W_e}{\sigma t \mu \Delta} \cdot$$ (2.3.26)

However, the skin depth is so small that the loss due to the tangential H field is the only one of significance. The total copper loss is then approximated by Equation (2.3.18).

The radiated power is found using the E field at the edge of the disk. From Equation (2.2.33), the field at the edge reduces to

$$E_z(a,\phi) = \frac{-j\omega\mu}{\pi K_1 a} \sum_{m=0}^{\infty} \frac{J_m(K_1\rho')\cos(m\phi)\sin(m\phi_w)}{J_m'(K_1 a)(1 + \delta_{mo})m\phi_w} ,$$ (2.3.27)

where ϕ is the azimuth angle with respect to the source. Using a Huygen's surface over the entire cavity, and assuming that negligible currents flow on the exterior surfaces of the copper boundaries,

$$\vec{K} = \hat{n} \times E_z \hat{z} ,$$ (2.3.28)

where $\vec{K}_s$ is an equivalent magnetic current ribbon.

24

The far field electric vector potential is well known to be

$$\vec{F} = \frac{-2e^{-jK_o r}}{4\pi r} \int_0^t \int_0^{2\pi} K_s e^{j(K_o \hat{r} - r')} \, ds' \, , \tag{2.3.29}$$

where the coordinate system is as in Figure 2.2 and the factor 2 accounts for the ground plane image. Assuming the thickness to be small gives

$$\vec{F} = \frac{-2te^{jK_o r}}{4\pi r} \int_0^{2\pi} K_s e^{jK_o\{x'\sin(\theta)\cos(\phi) + y'\sin(\theta)\sin(\phi)\}} \, ds' \, , \tag{2.3.30}$$

where the primed variables are source coordinates.

The vector potential can be found as the superposition of its rectangular components. Since

$$\vec{K}_s = K_s \hat{\phi} \, , \tag{2.3.31}$$

and

$$\hat{\phi} = -\hat{x}\sin(\phi') + \hat{y}\cos(\phi') \, , \tag{2.3.32}$$

then

$$\vec{F} = \frac{-jt\omega\mu e^{-jK_o r}}{2\pi^2 r K_1} \sum_{m=0}^{\infty} \frac{J_m(K_1\rho')\sin(m\phi_w)}{J_m'(K_1 a)(1 + \delta_{mo})m\phi_w}$$

$$\tag{2.3.33}$$

$$\cdot \int_0^{2\pi} \cos(m\phi)\{\hat{y}\cos(\phi') - \hat{x}\sin(\phi')\}e^{jK_o a\sin(\theta)\cos(\phi'-\phi)} \, d\phi' \, .$$

Letting

$$C(r) = \frac{-j2\omega\mu t e^{-jK_o r}}{4\pi^2 K_1 r} \quad \text{and} \quad \alpha = K_0 a \sin(\theta), \tag{2.3.34}$$

and using the fact that

$$e^{j\alpha \cos(\phi)} = \sum_{m=-\infty}^{\infty} (j)^m J_m(\alpha) e^{jm\phi}, \tag{2.3.35}$$

the far field vector potential reduces to

$$\begin{Bmatrix} F_x \\ F_y \end{Bmatrix} = -C(r) \sum_{m=0}^{\infty} \frac{J_m(K_1\rho') \sin(m\phi_w)}{J_m'(K_1 a)(1 + \delta_{m0})(m\phi_w)} \cdot$$

$$2 \sum_{n=0}^{\infty} (j)^n \frac{J_n(\alpha)}{(1 + \delta_{no})} \int_0^{2\pi} \begin{Bmatrix} \sin(\phi') \\ \cos(\phi') \end{Bmatrix} \cos(m\phi') \cos\{n(\phi' - \phi)\} \, d\phi'. \tag{2.3.36}$$

By the orthogonality of the cos $(m\phi)$, F_y and F_x reduce to

$$\begin{Bmatrix} F_x \\ F_y \end{Bmatrix} = C(r)\pi \left[J_0(\alpha) \begin{Bmatrix} 0 \\ \dfrac{J_1(K_1\rho)}{J_1'(K_1 a)} \end{Bmatrix} + \right.$$

$$\left. \sum_{n=1}^{\infty} (j)^n J_n(\alpha) \left[\frac{J_{n+1}(K_1\rho')}{J_{n+1}'(K_1 a)} - (1 + \delta_{n1}) \frac{J_{n-1}(K_1\rho')}{J_{n-1}'(K_1 a)} \right] \begin{Bmatrix} \sin(n\phi) \\ \cos(n\phi) \end{Bmatrix} \right], \tag{2.3.37}$$

and can be written more simply as

$$\begin{Bmatrix} F_x \\ F_y \end{Bmatrix} = \sum_{m=0}^{\infty} \begin{Bmatrix} R_m \sin(m\phi) \\ S_m \sin(m\phi) \end{Bmatrix}. \tag{2.3.38}$$

26

In the far field

$$\vec{E} = \nabla \times \vec{F} = -jK_o \hat{r} \times \vec{F} + 0\left(\frac{1}{r^2}\right) \ , \tag{2.3.39}$$

so that

$$\vec{E} = -jK_o \left\{ \hat{z} \sin(\theta) \left[\cos(\phi)F_y - \sin(\phi)F_x \right] \right.$$

$$\tag{2.3.40}$$

$$\left. + \hat{y} \cos(\theta)F_x - \hat{x} \cos(\theta)F_y \right\} \ .$$

In polar coordinates, the E field components are

$$E_\theta = \cos(\phi)F_y - \sin(\phi)F_x \qquad\qquad E_z = 0$$

$$\tag{2.3.41}$$

$$E_\phi = -\cos(\theta) \left[\cos(\phi)F_x + \sin(\phi)F_y \right] \ .$$

Once F_x and F_y' are known, the far electric field can be found for any ϕ and θ. From this, the radiation pattern can be calculated. The radiated power is found from

$$P_r = \frac{1}{n_o} \int_{\theta=0}^{\pi/2} \int_{\phi=0}^{2\pi} |E|^2 r^2 \sin(\theta)d\theta d\phi \ , \tag{2.3.42}$$

where

$$|E|^2 = E_x E_x^* + E_y E_y^* + E_z E_{\bar{z}}^* \ . \tag{2.3.43}$$

27

The integral over phi can be carried out in closed form. With orthogonality, the expression for the radiated power can be further reduced and the integral over θ can be numerically evaluated.

2.4 Input Impedance and the Distributed System

In general, the input impedance of a rigorously analyzed system can be found from

$$\frac{1}{Z_{in}} = \frac{P + j2\omega(W_e - W_m)}{V^2} \tag{2.4.1}$$

or

$$Z_{in} = \frac{P + j2\omega(W_e - W_m)}{I^2} \tag{2.4.2}$$

or even by

$$Z_{in} = \frac{V}{I} \quad . \tag{2.4.3}$$

Here, P is the power dissipated in the system, V is the driving point voltage, I is the source current, Z_{in} is the driving point impedance with no other ports on the disk, and W_e and W_m are the time-averaged electric and magnetic stored energies. However, for the disk antenna, the copper loss and radiated power are calculated using perturbation. Therefore, the above equations can not be expected to agree since the input voltage is insensitive to losses calculated in this way. In fact

28

the radiated power may be much larger than any other loss, so that the disagreement between the above equations can be severe.

An extremely efficient method for calculating the input impedance can be seen by considering that measurements show the microstrip antennas to have a high Q. Analytically, the quality factor of any system is defined as

$$Q = \frac{\omega \cdot \text{Stored Energy}}{\text{Total Power Loss}} \qquad (2.4.4)$$

Since the measured Q is very high, the origin of the power loss is unimportant. This indicates that the losses can be redistributed with little effect on the internal field structure. Since the input voltage is directly related to the E field at the feed, Equation (2.4.3) indicates that the input impedance will be relatively unaffected by such a power loss redistribution. This result may be paralleled by the simple high Q RLC tank circuit whose input impedance is nearly independent of where the loss occurs.

Once the copper, dielectric, and radiated power losses have been calculated as in Section 2.3, they can be distributed throughout the dielectric. The system will then consist of a perfect cavity with a modified lossy dielectric.

The losses are redistributed by modifying the dielectric loss tangent. From Equation (2.3.9), the modified loss tangent is defined as

$$\delta_{eff} = \frac{P_{cu} + P_d + P_r}{2\omega W_e} \qquad . \qquad (2.4.5)$$

29

The complex wave number for the modified dielectric is then

$$K_{1_{eff}} = \omega \sqrt{(1 - j\delta_{eff})\mu\epsilon} \qquad (2.4.6)$$

and the E field can be reexpanded using Equation (2.2.33). The input impedance is then efficiently evaluated using Equation (2.4.3).

The input voltage can be found using the E field from either of regions 1 and 2, and the fact that

$$V = \vec{E} \cdot \hat{z}t \; . \qquad (2.4.7)$$

However, since the voltage is averaged over the feed width (due to the presence of the feed conductor), the final expression for the input voltage is

$$V_{in} = t \sum_{m=0}^{\infty} C_m J_m(K_{1_{eff}}\rho') \frac{\sin^2(m\phi_w)}{(m\phi_w)^2} \; . \qquad (2.4.8)$$

It is interesting to note that the quality factor of the disk antenna is just the reciprocal of the effective loss tangent. Indeed,

$$Q = \frac{\omega(W_e + W_m)}{P_T} \; . \qquad (2.4.9)$$

However, $W_e = W_m$ at resonance. Thus, Equation (2.4.5) gives

$$Q = \frac{2\omega W_e}{P_T} = \frac{1}{\delta} \; . \qquad (2.4.10)$$

30

This relationship can lead to some major computational savings since the quality factor is relatively independent of the feed location. Near the m-th resonance, where one term dominates all others, it is clear that

$$E(\rho=a) \propto \frac{J_m(K_1\rho')}{J_m{'}(K_1a)} \quad . \tag{2.4.11}$$

But the radiated power is proportional to the square of the electric field at the disk edge so that

$$P_r \propto \left[\frac{J_m(K_1\rho')}{J_m{'}(K_1a)} \right]^2 \quad . \tag{2.4.12}$$

Also

$$W_e \propto \left[\frac{J_m(K_1\rho')}{J_m{'}(K_1a)} \right]^2 \quad , \tag{2.4.13}$$

with both copper and dielectric losses being proportional to W_e. Therefore, as long as the resonant term dominates all others in magnitude, the effective loss tangent will remain nearly constant. This indicates that one effective loss tangent can be used to find the input impedance for any feed location where the dominant mode is excited. The same loss tangent can be used for any frequency near resonance since one mode is still dominant. This means that the radiated power and electric stored energy have to be calculated only once for all of those data points. The magnetic stored energy is never needed since the input impedance is equivalent to the driving point voltage when the source

31

current is assumed to be one ampere.

2.5 The Disk Antenna with Two Ports

The general multiple-port disk of Figure 2.5 can be used as one of many elements in an array of microstrip antennas. Another use for multiple ports is in exercising some form of mode control by placing shorting studs (short circuited ports) about the disk. The input impedance of a multiple-port disk can be approximated by using the simple model of the previous analysis. However, for simplicity, only the two port disk is analyzed here since the analysis readily generalizes to any number of ports.

A two-port network is described by

$$
\begin{bmatrix} V_1 \\ V_2 \end{bmatrix} = \begin{bmatrix} Z_{11} & Z_{12} \\ Z_{21} & Z_{22} \end{bmatrix} \begin{bmatrix} I_1 \\ I_2 \end{bmatrix} ,
\tag{2.5.1}
$$

where the currents are directed into each port. The open circuit Z parameters have been chosen since all are calculated with one of the port currents equal to zero. For the simple cavity, a port with no current is the same as no port at all, so that each parameter reduces to a one-port calculation. The Z parameters are

$$
Z_{ij} = \frac{V_i}{I_j} \Bigg|_{I_k = 0, \ k \neq j}
\tag{2.5.2}
$$

so that Z_{in} is equivalent to the voltage that exists at the location of the i-th port with that port removed (when I is taken as a one ampere
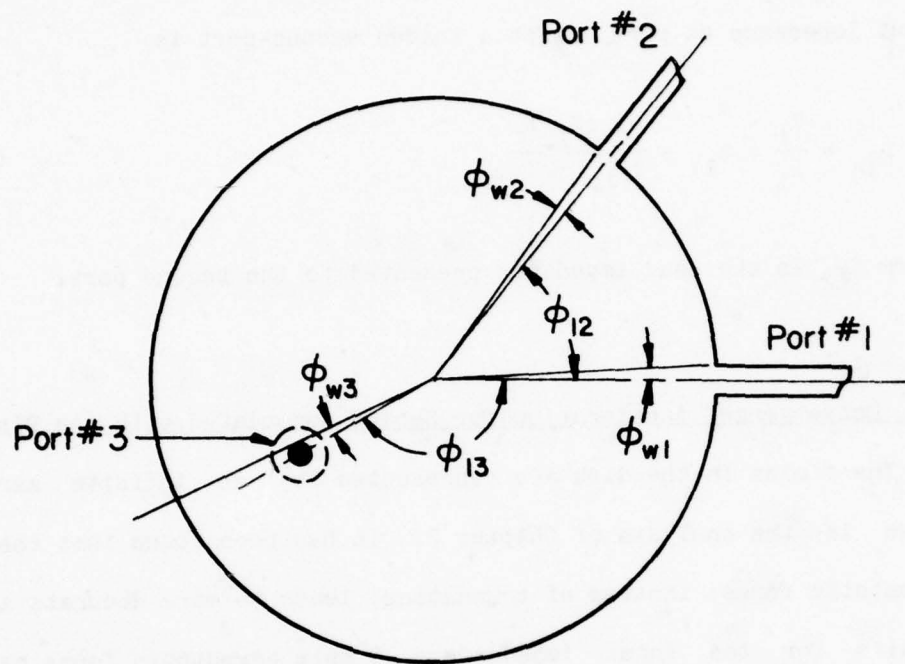
32

Figure 2.5. A general multiport disk antenna.

33

source). From equation (2.2.33), the voltage is known for any location on the disk, and by reciprocity, $Z_{12} = Z_{21}$. From Equation (2.5.1), the input impedance at port 1 with a loaded second-port is

$$Z_{in} = \frac{V_1}{I_1} = Z_{11} + \frac{(Z_{12})^2}{(Z_{L2} - Z_{22})} \quad .$$

(2.5.3)

where Z_{L2} is the load impedance presented to the second port.

2.6 Convergence Acceleration for Series Associated with the Disk

The fields in the disk are represented by an infinite series as shown in the analysis of Chapter 2. It has been found that the use of asymptotic forms, instead of truncation, leads to more accurate analytic results for the input impedance. Simple asymptotic forms have been found for both the input voltage and the electric stored energy. Radiation due to the non-resonant modes is negligible so that an asymptotic form need not be found for the radiated power.

The advantage of using the asymptotic forms for the tail of a series is that a closed form expression, or one which converges more rapidly than the original form, can often be found. Using Khummer's well known transformation, any series S, as in

$$S_1 = \lim_{p \to \infty} \sum_{m=1}^{p} \Lambda_m$$

(2.6.1)

can be rewritten as

$$S_2 = \lim_{p \to \infty} \sum_{m=1}^{p} \left[A_m - \lambda_m \right] + \sum_{m=1}^{\infty} \lambda_m , \qquad (2.6.2)$$

where the A_m and λ_m are the actual and asymptotic terms respectively. As indicated, when the upper limit (P) tends to infinity the sums S_1 and S_2 become identical. However, by using Khummer's transformation, the rate of convergence has been greatly increased. Therefore, truncation of S_2 will cause less error than the truncation of S_1.

Investigation of the equations for the internal fields shows that the asymptotic terms must use the large order approximations for the Bessel functions. For large m, the Bessel functions have asymptotic forms of

$$J_m \sim \frac{1}{\sqrt{2\pi m}} \left(\frac{\varepsilon z}{2m} \right)^m ,$$

$$\qquad (2.6.3)$$

$$Y_m \sim - \frac{2}{\sqrt{\pi m}} \left(\frac{\varepsilon z}{2m} \right)^{-m} .$$

From Section 2.2, the electric fields in regions 1 and 2 of Figure 2.4 are known. Substituting the asymptotic forms for the Bessel functions gives

$$E_{z1 \ m} \sim \frac{-j\omega\mu}{2\pi m} \left[\frac{\rho'}{a} \right]^m \left\{ \left[\frac{\rho}{a} \right]^m + \left[\frac{a}{\rho} \right]^m \right\} \frac{\cos(m\phi) \ \sin(m\phi_w)}{(m\phi_w)}$$

$$\qquad (2.6.4)$$

$$E_{z2 \ m} \sim \frac{-j\omega\mu}{2\pi m} \left[\frac{\rho}{a} \right]^m \left\{ \left[\frac{\rho'}{a} \right]^m + \left[\frac{a}{\rho'} \right]^m \right\} \frac{\cos(m\phi) \ \sin(m\phi_w)}{(m\phi_w)} .$$

35

In simplifying to these final forms, the relations

$$e = \lim_{m \to \infty} \left[\frac{m + 1}{m} \right]^m \qquad \text{and} \qquad \lim_{m \to \infty} \left[\frac{m - 1}{m} \right]^m = 0 \qquad (2.6.5)$$

were used. The asymptotic form for the electric stored energy is found from Equations (2.6.5) and (2.2.33) to be

$$\left(W_e \right)_m \sim \frac{\varepsilon_o \varepsilon_r}{4\pi^2} \left\{ \frac{(\rho')^2}{m} \left[1 + \left(\frac{\rho'}{a} \right)^{2m} \right] + 2(a - \rho') \left(\frac{\rho'}{a} \right)^{2m} \right\} \frac{\sin^2(m\phi_w)}{m^4 \phi_w} \quad . \qquad (2.6.6)$$

This is largest when $\rho' = a$, or

$$\left(W_e \right)_m \sim \frac{\varepsilon_o \varepsilon_r a^2}{2\pi^2} \left[\frac{\sin^2(m\phi_w)}{m^5 \phi_w} \right] \quad . \qquad (2.6.7)$$

Even for this largest case, ϕ_w is always large enough so that the $(W_e)_m$ diminish rapidly with increasing m. Therefore, Equation (2.6.1) is used to calculate the electric stored energy. Since convergence is very rapid, the series is simply truncated at some order N. In the actual computer program, the series was truncated when the last term added was less than .05% of the accumulated total.

The asymptotic expressions for the Z parameters are found from Equation (2.6.4). As pointed out in Section 2.5, the Z parameters all reduce to voltages which, in turn, reduce to electric fields. Averaging the voltage across the feed width gives a Z_{11} with asymptotic form

$$\left(Z_{11} \right)_m \sim \frac{-j\omega\mu t}{2\pi m} \left[\left(\frac{\rho'}{a} \right)^{2m} + 1 \right] \left[\frac{\sin(m\phi_w)}{m\phi_w} \right]^2 \quad . \qquad (2.6.8)$$

36

For the cross-port parameters, the asymptotic form is different for the two regions of the disk. When $\rho_i > \rho_j$ (where the j-th port is the source port),

$$\left(z_{ij}\right)_m \sim \frac{-j\omega\mu t}{2\pi m} \left[\frac{\rho_i{}'\rho_i{}'}{a^2} + \frac{\rho_j{}'}{\rho_i{}'} \right] \frac{\cos(m\phi_{ij}) \sin(m\phi_{wi}) \sin(m\phi_{wj})}{m^2 \phi_{wi}\phi_{wj}} \quad (2.6.9)$$

Otherwise, the ρ_j / ρ_i term is inverted. Inspection of these equations shows that the rate of convergence decreases as ρ_i approaches ρ_j, and as both ρ_i and ρ_j approach a.

Rapidly converging forms can easily be found for these asymptotic expressions when $\rho_i = \rho_j = a$, or when $\rho_i = \rho_j$. For these cases, at least one term in the brackets of Equation (2.6.9) is identically 1. For that term, the sum of the asymptotic series can be evaluated quite rapidly, using Clausen's integral. Indeed,

$$\sum_{m=1}^{\infty} \frac{\sin(m\phi_{w1}) \sin(m\phi_{w2}) \cos(m\phi_{12})}{m^3 \phi_{w1}\phi_{w2}} = \frac{1}{4\phi_1\phi_2} \left[\sum_{m=1}^{\infty} \frac{\cos\{m(\phi_{w1} - \phi_{w1} - \phi_{12})\}}{m^3} \right.$$

$$+ \sum_{m=1}^{\infty} \frac{\cos\{m(\phi_{w1} - \phi_{w2} + \phi_{12})\}}{m^3} \quad (2.6.10)$$

$$+ \sum_{m=1}^{\infty} \frac{\cos\{m(\phi_{w1} + \phi_{w2} - \phi_{12})\}}{m^3} + \left. \sum_{m=1}^{\infty} \frac{\cos\{m(\phi_{w1} + \phi_{w2} + \phi_{12})\}}{m^3} \right] .$$

But, each of the above sums is known to be the integral of Clausen's integral, found in any major handbook. Numerical evaluation of these sums is straightforward and is outlined in Appendix C.

When the radial feed locations are not equal, the series of (2.6.8) and (2.6.9) converge at least as fast as a geometric series. For these

cases, Z_{ij} is evaluated as in Equation (2.6.1). However, for cases where the radial feed locations are nearly but not quite equal, the form

$$Z_{ij} \doteq \sum_{m=0}^{p} A_m + \sum_{m=p}^{q} \lambda_m \qquad (2.6.11)$$

is used to obtain Z_{ij} since the λ_m are easier to evaluate than the A_m.

CHAPTER 3

ANALYTIC AND EXPERIMENTAL RESULTS

3.1 Determination of δ and σ To analyze the microstrip disk, the copper
conductivity and dielectric loss tangent must be specified. The
conductivity of copper is well known to be 580 Kmho-cm, and the
dielectric loss tangent is given by the manufacturer of the dielectric
in the form of a frequency dependent graph. For convenience, it is
partially reproduced in Figure 3.1. However, when using these values to
calculate the input impedance locus, the results are substantially in
error.

To illustrate the point, a microstrip disk with a radius of 6.7 cm
and a thickness of 1.5 mm was fed at a radius of 3.35 cm, and analyzed.
The theory indicates the lowest resonance to be near 810.61 MHz since
this is where the first minimum of $J_n{}'(K_1 a)$ occurs. For this frequency
the loss tangent is given by the manufacturer as 0.00085. The Smith
chart locus for Z_{11} was calculated using the manufacturer's loss tangent
and the conductivity given above. For comparison, the calculated and
measured results are shown in Figure 3.2. These results indicate that
more loss exists in the system than the theory presently accounts for.
At this point it was decided that the copper loss and loss tangent
should be determined experimentally.

To experimentally determine σ and δ, a bona-fide rectangular
cavity was constructed by closing the radiating aperture with copper
foil, as in Figure 3.3. With the bona-fide cavity, the effective loss

39
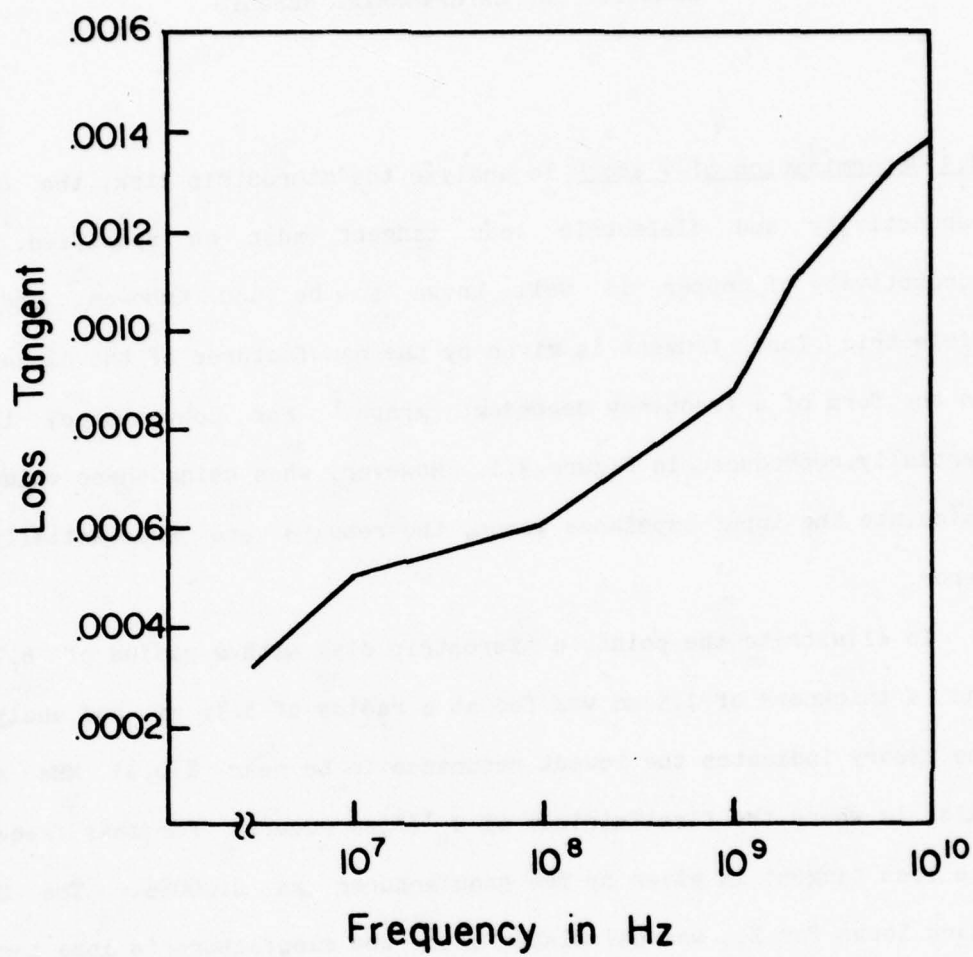
Figure 3.1. Manufacturers loss tangent data for Rexolite 2200
(Atlantic Laminates).

a=6.7 cm.
t=0.15 cm.
ε_r=2.62
δ=.00085
σ=580 K℧ cm.

+   +   computed points
5.0 MHz   increment

○────○   measured locus
5.0 MHz   increment
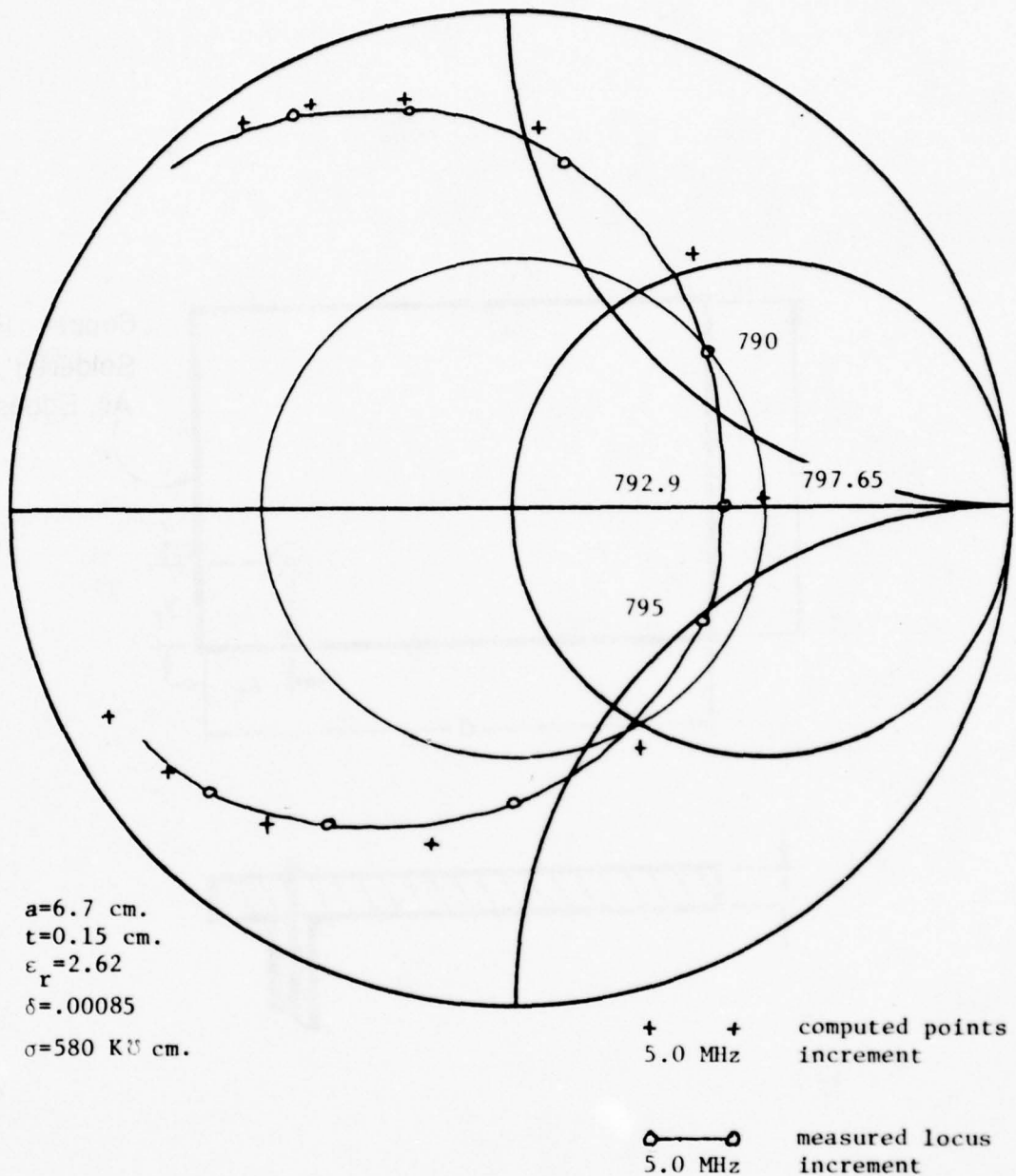
Figure 3.2.   A set of input impedance results using the
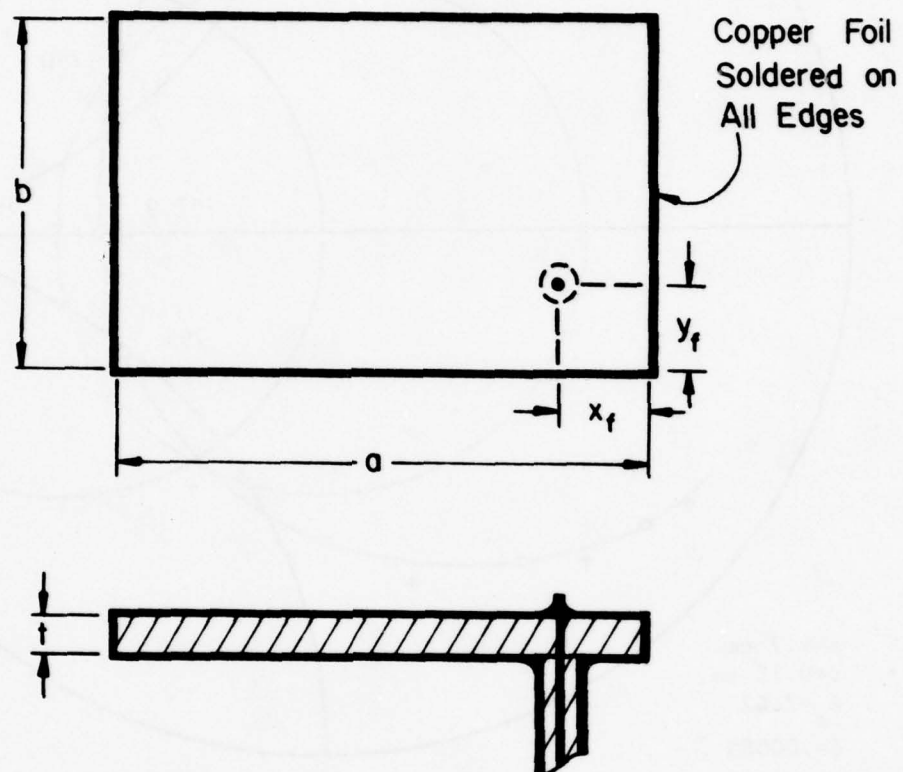manufacturer's loss tangent value, and the
standard copper conductivity.

Figure 3.3. The bona-fide cavity used to measure the loss
tangent and the copper conductivity.

tangent is

$$\delta_{eff} = \frac{(P_{cu} + P_d)}{2\omega W_e} , \tag{3.1.1}$$

where the radiated power has been eliminated. The resonant Q is still
given by

$$Q = \frac{1}{\delta_{eff}} . \tag{3.1.2}$$

Since P_{cu} and δ are given at resonance by

$$P_{cu} = \frac{2\omega W_e \Delta}{2t} \qquad \text{and} \qquad \frac{1}{\delta} = \frac{2 W_e}{P_d} , \tag{3.1.3}$$

Equation (3.1.1) leads to

$$\frac{1}{Q} = \delta + \frac{\Delta}{2t} . \tag{3.1.4}$$

The quality factor and dielectric thickness can be measured, leaving δ
and Δ (the skin depth) as two unknowns. By constructing two similar
cavities with different thicknesses, and measuring their quality
factors, δ and Δ can be determined from the resulting simultaneous
equations. Although Equation (3.1.3) neglects the loss in the copper
foil used to seal the cavity, it is assumed that this extra loss is
negligible since the cavity thickness is much smaller than any other
dimension.

Once the skin depth is determined as above, the conductivity is found from the relation

$$\Delta = \sqrt{\frac{2}{\omega\mu\sigma}} \tag{3.1.5}$$

Unfortunately, the manufacturer's data indicate that the loss tangent (for the Rexolite 2200 dielectric) varies with frequency. For this reason, δ and σ must be redetermined when the frequency is changed substantially.

The rectangular cavity experiment was performed for a resonant frequency near 428.00 MHz and the results are shown in Figure 3.4. The intersecting lines are each generated by

$$\delta = \frac{1}{Q} - \frac{\Delta}{2t} \tag{3.1.6}$$

With the materials available, cavity thicknesses of 1.5 mm and 4.5 mm were constructed. Unfortunately, these thicknesses give a set of equations that is not well conditioned. Because of this, the Q was measured several times. The locus of points for the upper and lower limits of Q were then plotted. In Figure 3.4, the resulting region of intersection shows the uncertainty of δ and σ. From the centroid of the shaded area, $\delta = .00083$ and $\Delta = 9.2$ μm. From Equation (3.1.5), $\sigma = 69.9$ **Kmho-cm**. This method can be performed for each resonant frequency.

From these results the effective conductivity is much lower than the table value. This discrepancy may be due to surface roughness or
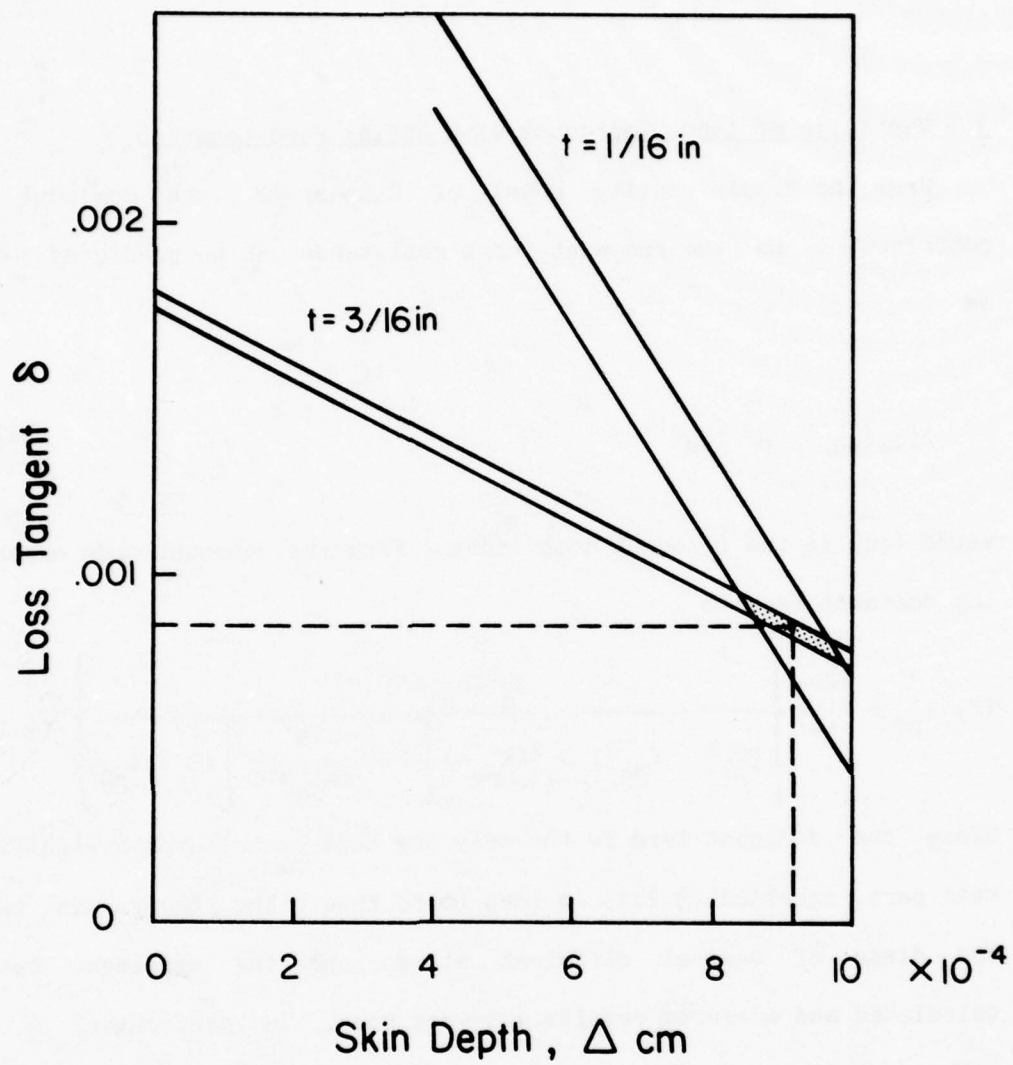
Figure 3.4. Experimental results for the determination of the loss tangent and the copper conductivity.

possibly to a lossy bonding agent.

3.2 Variation of Input Impedance with Radial Feed Location

From the simple cavity model of Chapter 2, the dominant term contribution to the resonant input resistance can be predicted to vary as

$$(Z_{11})_{pq} = J_p^{\,2}(K_{pq}\rho') \,, \tag{3.2.1}$$

where (pq) is the resonant mode index. From the resonant mode expansion the dominant term is

$$(Z_{11})_{pq} = \frac{j2\omega\mu}{\pi a^2}\left\{ \frac{J_q^{\,2}(K_{pq}\rho')}{(K_1^{\,2} - K_{pq}^{\,2})\, J_q^{\,2}(K_{pq}a)\left[1 - \dfrac{q^2}{(K_{pq}a)^2}\right](1 + \delta_{p0})} \right\} \tag{3.2.2}$$

Since the dominant term is the only one that contributes a significant real part, equation (3.2.1) is seen to be true. The theory was tested for disks of several different sizes, and the agreement between calculated and measured results was very good. In particular, a disk with a radius of 6.7 cm and a dielectric thickness of 1.5 mm was coaxially fed at the different points of Figure 3.5. For the analysis, a dielectric loss tangent of 0.00135 and a copper conductivity of 80.2 Kmho-cm were used, based on the measured cavity results of Section 3.1. The feed width was taken to be the diameter of the coaxial center conductor. Some of the more interesting input impedance loci are shown in Figure 3.6. The resonant input resistance is plotted against radial

46
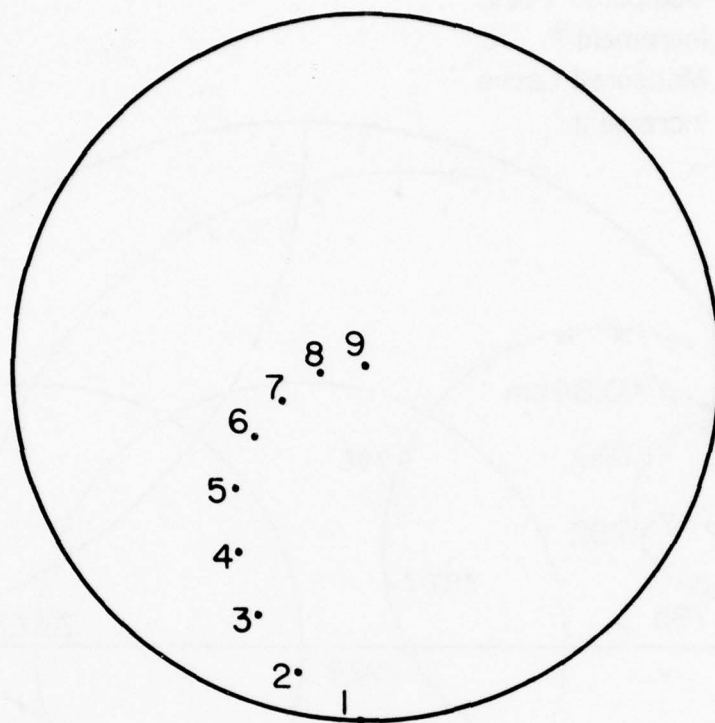
Figure 3.5.   Feed location used to determine the variation
of the resonant input impedance with radial
feed location.

×   ×   Computed Points
2.5 MHz   Increment ✳
o———o   Measured Locus
5.0 MHz   Increment

$\rho' = 0.84$ cm

790

797.7 792

795

790

797.7

792.8

795

790

797.7

792.8

795

$\rho' = 1.68$ cm

$\rho' = 5.03$ cm

✳ Computed Point
Increment 5.0 MHz

a = 6.7 cm

t = 0.15 cm

ϵ_r = 2.62

δ = 0.00135

σ = 80.2 KΩ/cm
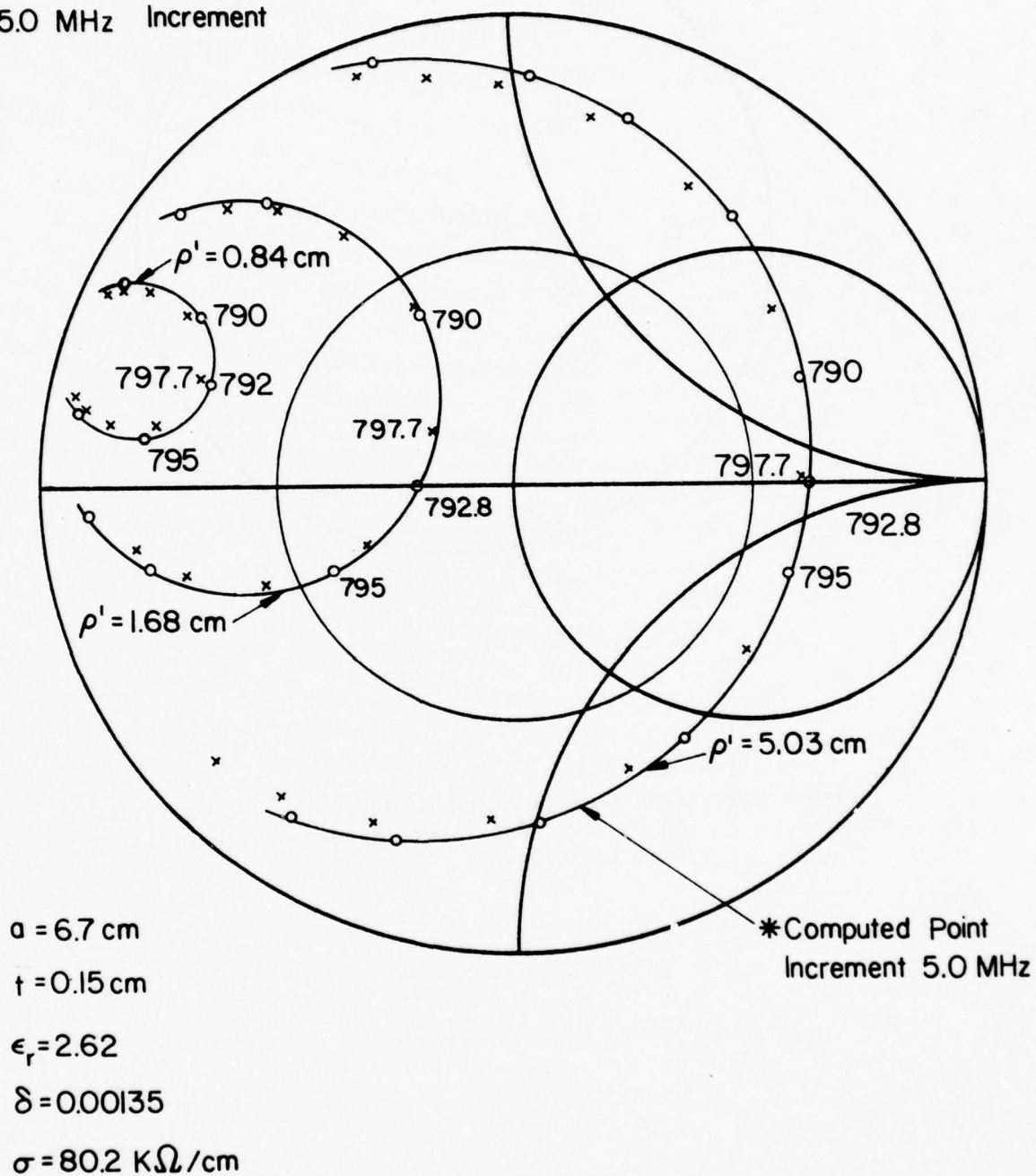
Figure 3.6.   Calculated and measured first-mode input
impedance loci for several radial feed
locations on the disk.

48

feed location for all eight feed points, as shown in Figure 3.7. As seen, the calculated and measured results are in excellent agreement.

For the lowest frequency mode, the cavity model of Chapter 2 has been successful at predicting both the resonant input resistance and the shift of the entire locus above the real axis of the Smith chart. However, for the higher frequency resonances, the theory predicts too much added positive reactance, although the measured and calculated resonant input resistances still agree very well. Some results for the second resonance of the disk of Figure 3.5 are shown in Figure 3.8. The theory predicts too much shift above the real axis, regardless of the radial feed location. In Figure 3.9 the resonant input resistance is plotted against radial feed location for both measured and calculated data. This Figure shows very good agreement and indicates that the losses are correctly accounted for. For a given radial feed location, the added reactance is a function of the feed width, as Equation (2.6.4) indicates. By increasing the feed width from the value that gave good results at the first resonance, the results from the higher resonances can be made to agree in the amount of locus shift, without changing the resonant resistance.

As mentioned in Chapter 2, no attempt has been made to satisfy the boundary condition that E_z be zero at the surface of the coaxial center conductor. It may be that this has contributed more error to the higher frequencies than to the lower.

The results for the higher resonances indicate that the effective feed width of the coaxial line needs investigation. From the boundary condition at the center conductor, the electric field near the feed has

49
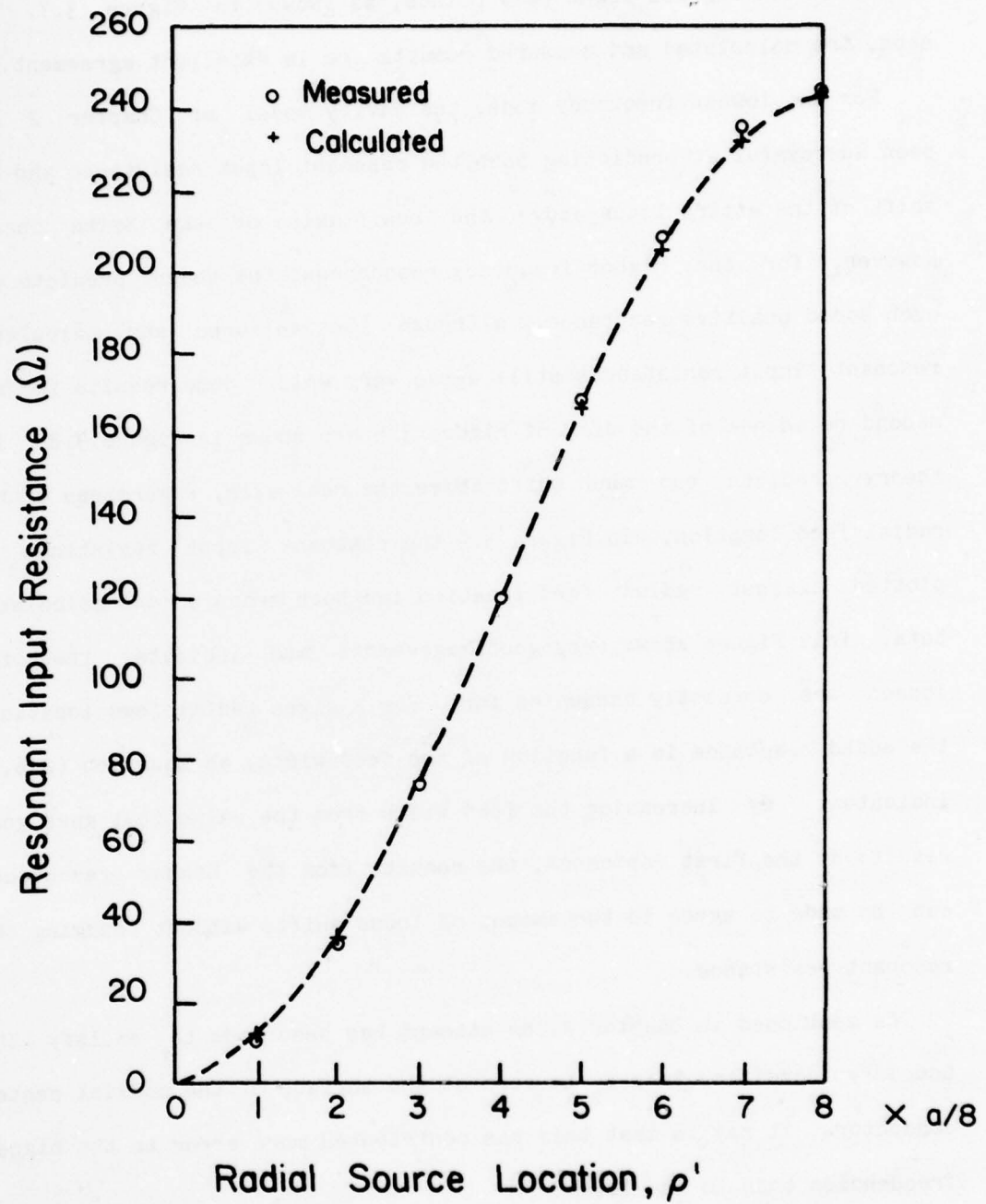
Figure 3.7. The variation of first-mode resonant input
resistance with radial feed location.
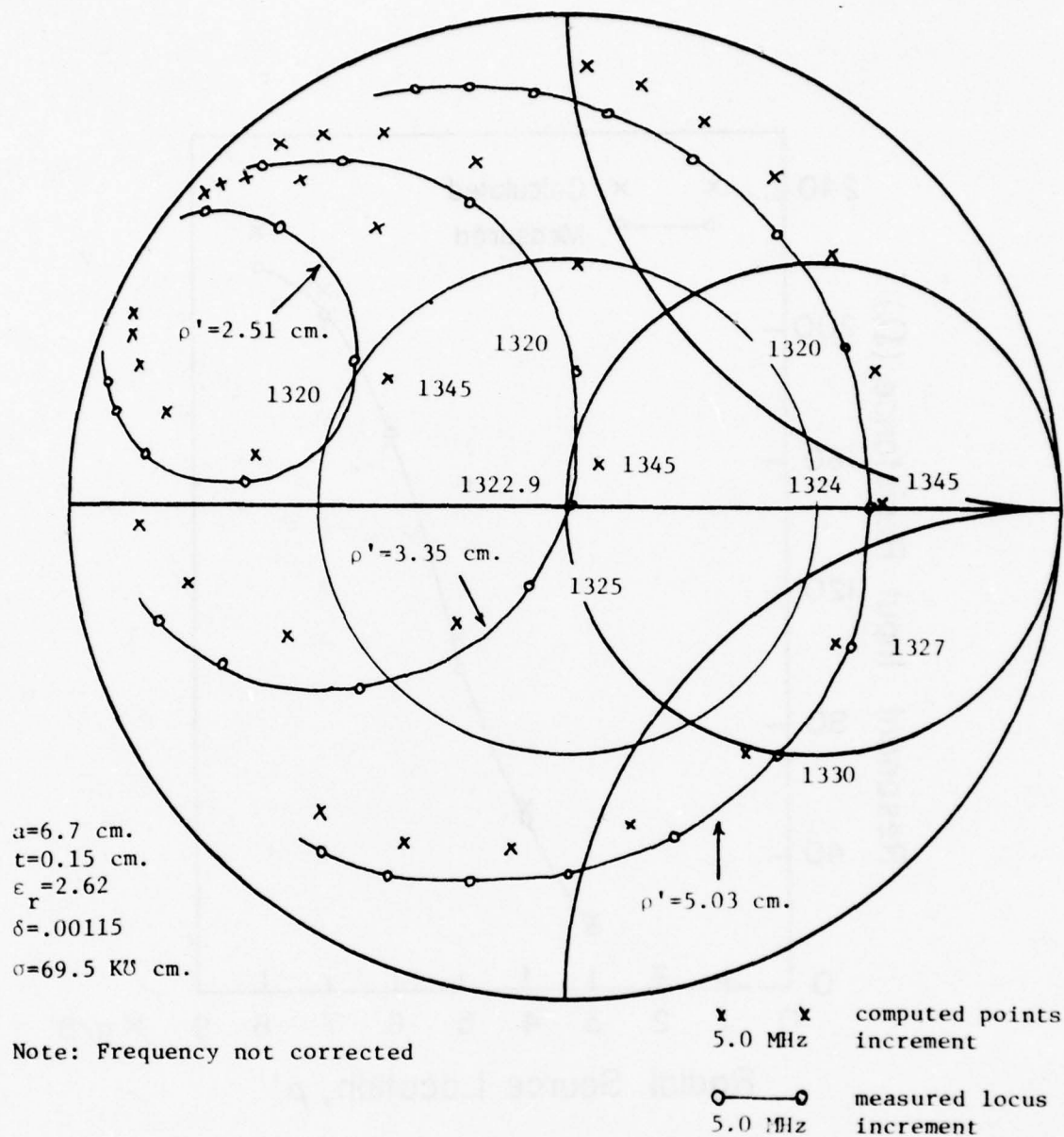
Figure 3.8.   Calculated and measured second-mode input
impedance loci for several feed locations
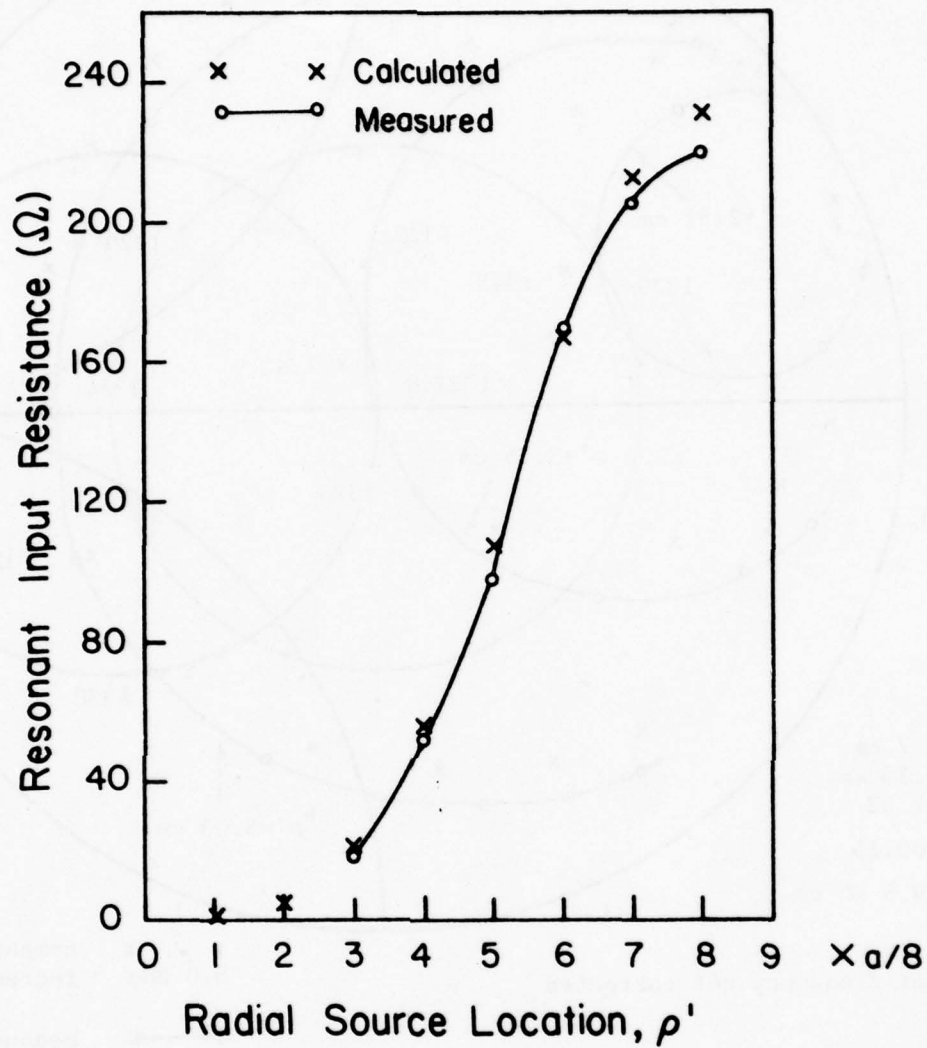on the disk.

Figure 3.9.   The variation of second-mode resonant input
resistance with radial feed location.

the form shown in Figure 3.10. It is not easy to see how this field distortion affects the input impedance contribution of each mode. For the high-order modes, the coaxially fed antenna may have to be considered as two coupled coaxial cavities as suggested in Section 2.3.

3.3 Variation of Input Impedance with Shorting Stud Location

One disadvantage of the single-port disk antenna is that the feed must be taken inside the disk to vary the input impedance. Consequently, the feed must be coaxial. In an array of such antennas, it would be more convenient to feed each antenna with a microstrip line. This would eliminate a lot of unwanted coaxial cabling behind the antennas.

The simple cavity model predicts that a two-port disk antenna can be edge-fed and still have a variable input impedance such as that discussed in Section 3.2. From Equation (2.5.3), if the second port is shorted then

$$Z_{in} = Z_{11} - \frac{(Z_{12})^2}{Z_{22}} \quad . \tag{3.3.1}$$

Considering the dominant mode contribution, this is

$$Z_{in} = A_{pq} \left[J_p^{\ 2}(K_{pq}\rho_1{}') - J_p^{\ 2}(K_{pq}\rho_2{}')\cos^2(m\phi_{12}) \right] \frac{\sin^2(m\phi_{w1})}{(m\phi_{w1})} \quad . \tag{3.3.2}$$

If both ports are at the same radius, then
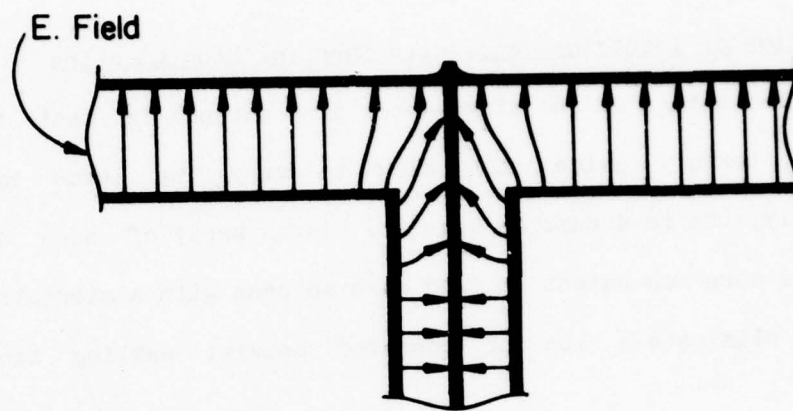
Figure 3.10.   The electric field near a coaxial field.

$$Z_{in} \propto J_p^2(K_{pq}\rho') \sin^2(m\phi_{12}) \quad . \tag{3.3.3}$$

Thus, the resonant input resistance is seen to vary with radius and with separation of the two ports. For the edge-fed case,

$$Z_{in} \propto J_p^2(K_{pq}a) \sin^2(m\phi_{12}) \quad , \tag{3.3.4}$$

where the shorting stud is also on the edge.

Equation (3.3.4) was tested with a microstrip-fed antenna, with a radius of 12.68 cm. The first mode resonance is near 420 MHz. Figure 3.11 shows the disk and the set of short locations used. Some interesting impedance loci are shown in Figure 3.12. Although the calculated shift of each locus is incorrect, the resonant input resistances match very well. Figure 3.13 shows the plot of maximum input resistance versus separation angle, ϕ_{12}. The agreement is shown to be very good, but the fact that the impedance loci are shifted incorrectly indicates that the feed width of the first and second ports may need to be modified.

Another interesting result of the two-port antenna is that additional poles are introduced into the system where $Z_{L2} = Z_{22}$, as Equation (2.5.3) indicates. For convenience that equation is repeated below.
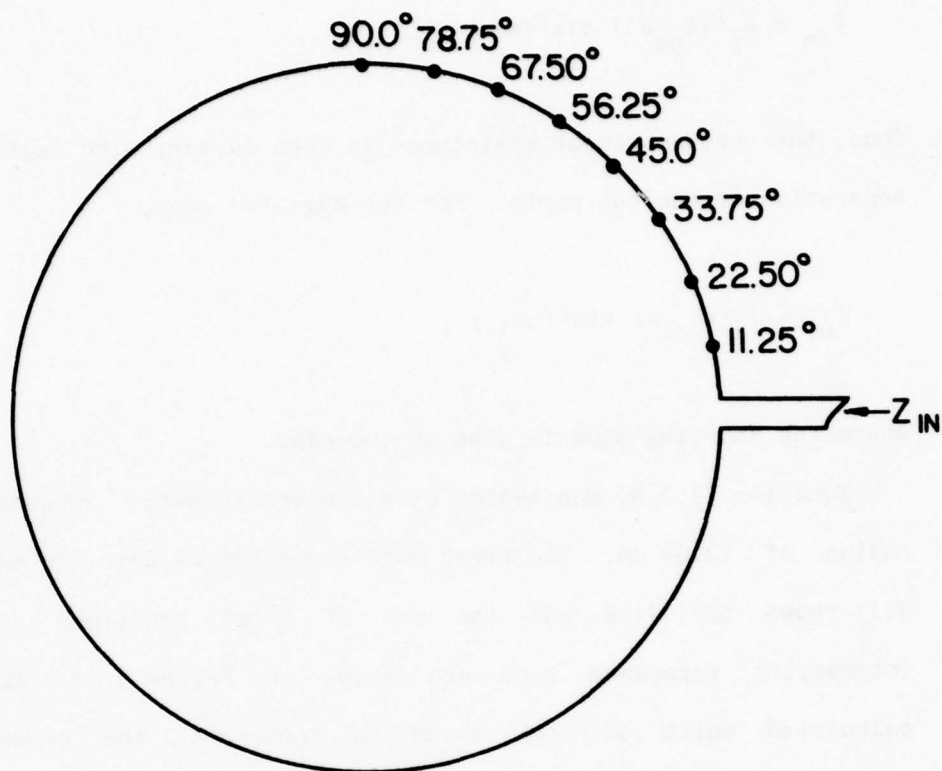
Figure 3.11. Short locations used to determine the variation of resonant input resistance with angular separation of the feed port and shorting stud.

56
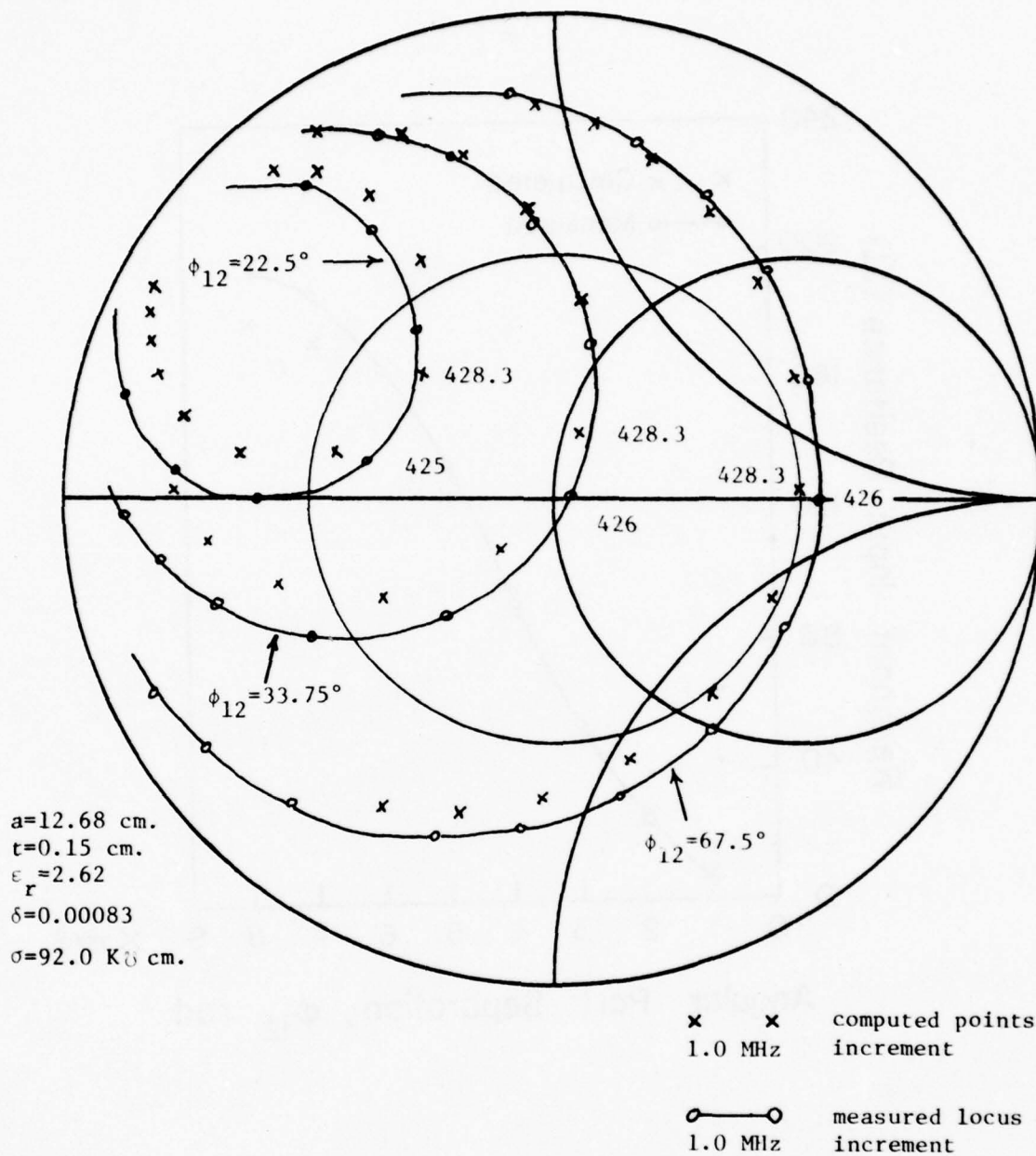
Figure 3.12. Calculated and measured input impedance loci
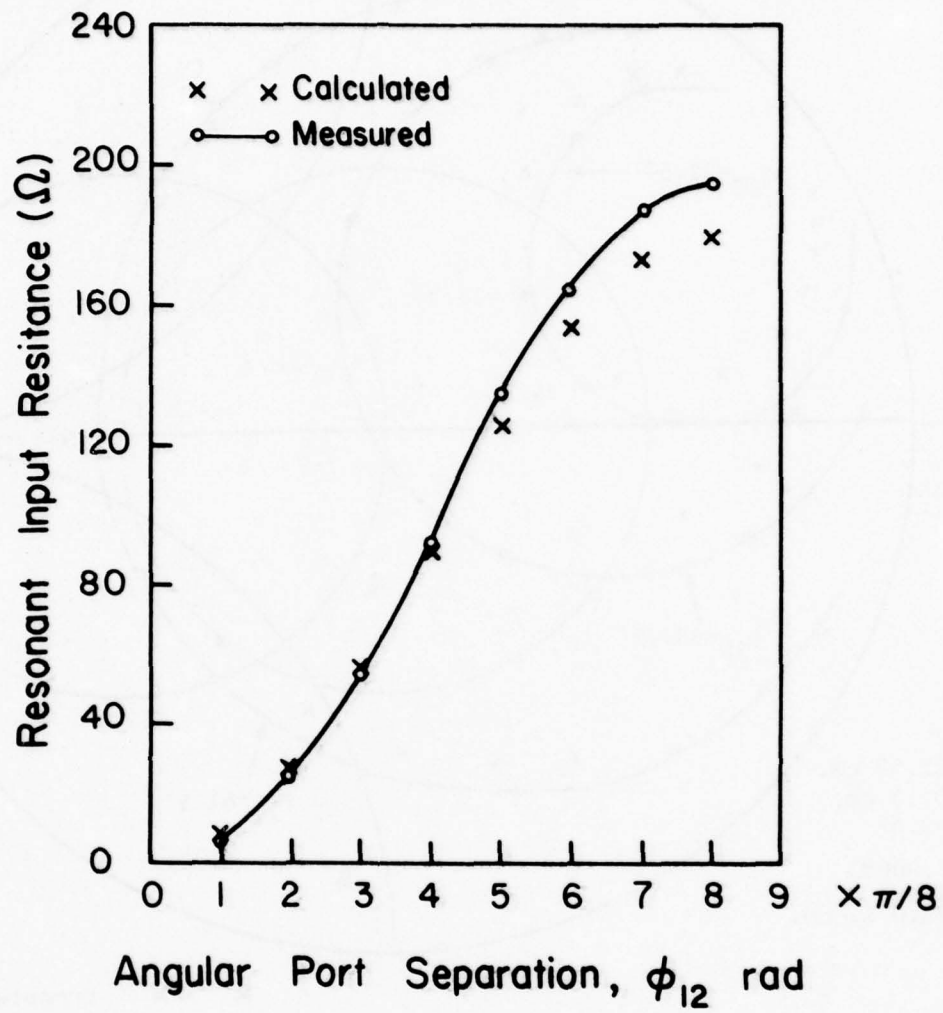for several feed port and shorting stud
separation angles.

Figure 3.13. The variation of resonant input impedance with angular separation of the feed port and the shorting stud.

$$Z_{in} = Z_{11} + \frac{(Z_{12})^2}{(Z_{L2} - Z_{22})} \quad . \tag{3.3.5}$$

When Z_{L2} is a short circuit, a resonance should occur near where Z_{22} passes through zero. However, for an edge fed disk, Z_{22} is equal to Z_{11} when the feed widths are the same. Note that the "zero" impedance at port 2 is converted to a "pole" at port 1. This was verified both experimentally and analytically. For the disk of Section 3.2, the first resonance of Z_{22} occurs at 810.61 MHz. However, as shown in Figure 3.14, the single-port input impedance first passes near zero at about 860 MHz. The result of positioning a short circuited port at $\phi = 45°$ is also shown in the figure. It is seen from the figure that a second resonance has occurred near 860 MHz, as predicted by the theory. That this resonance can be useful is shown in Section 3.5, where the radiation pattern is investigated.

3.4 A Circuit Model For the Disk Input Impedance

In the analysis of the disk, it was shown that mode matching and a resonant mode expansion give identical results for the simple cavity model. From the resonant mode expansion, it is seen that the input impedance for a one-port disk near resonance is

$$Z_{11} = \frac{j\omega A_{pq}}{K_1^2 - K_{mn}^2} + \text{(non-resonant terms)} , \tag{3.4.1}$$

where (pq) is the resonant mode index. Near resonance, the first term

59
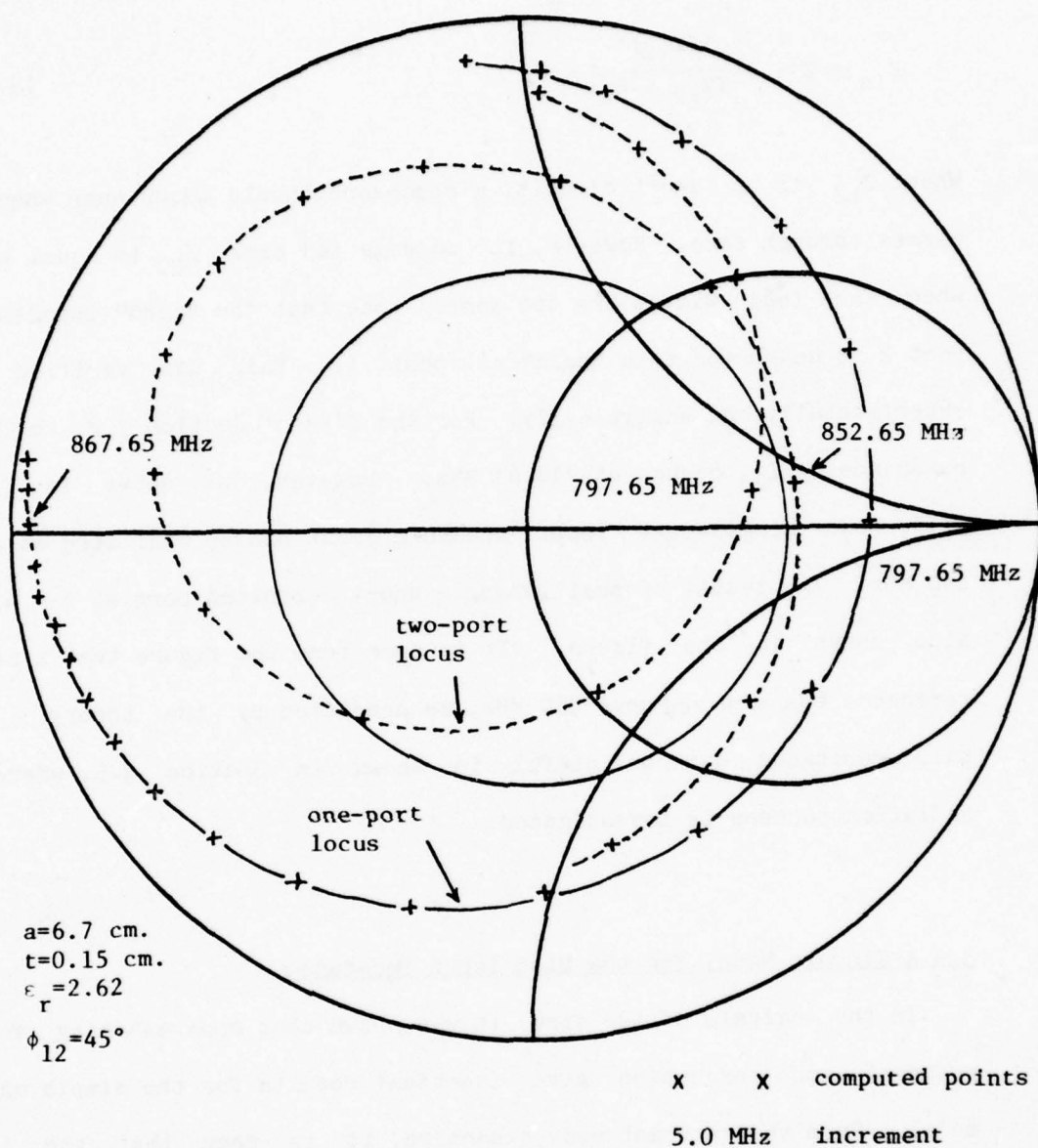
Figure 3.14. Two impedance loci showing the zero-to-pole conversion caused by a shorting stud 45 degrees from the feed port.

in the above equation dominates all of the rest. Considering the
dominant term alone, the input admittance has a nearly constant
conductance over the usable bandwidth, as does a parallel RLC tank
circuit. The Smith chart locus for such a contribution is shown in
Figure 3.15.

The analysis of Section 2.6 gave an asymptotic form for the
high-order non-resonant modes, in terms of the mode matching results.
From Equation (2.6.10) and any handbook on Clausen's integral, it is
evident that the sum of the higher-order non-resonant asymptotic terms
contributes a positive reactance to the input impedance. Experimental
results show that the input impedance locus is nearly a perfect circle
and is always shifted toward inductive reactance for the resonances that
the laboratory equipment is able to examine. The result would seem to
be that the sum of all of the non-resonant terms, including the
lower-order ones, contributes a positive reactance to the input
impedance.

Since the frequency band of interest is very narrow, the positive
reactance can be approximated as a linear function of frequency, and
thus as an inductive reactance. Adding this inductive reactance to the
dominant mode impedance gives the shifted locus in Figure 3.15.

In Sections 3.2 and 3.3, it was shown that the resonant input
resistance of the dominant mode contributions of the one-port and
two-port disks could be varied by changing the port locations. This
behavior is quite like that of a tapped RLC tank circuit, where the tap
location is changed. Considering these results, a simple circuit model
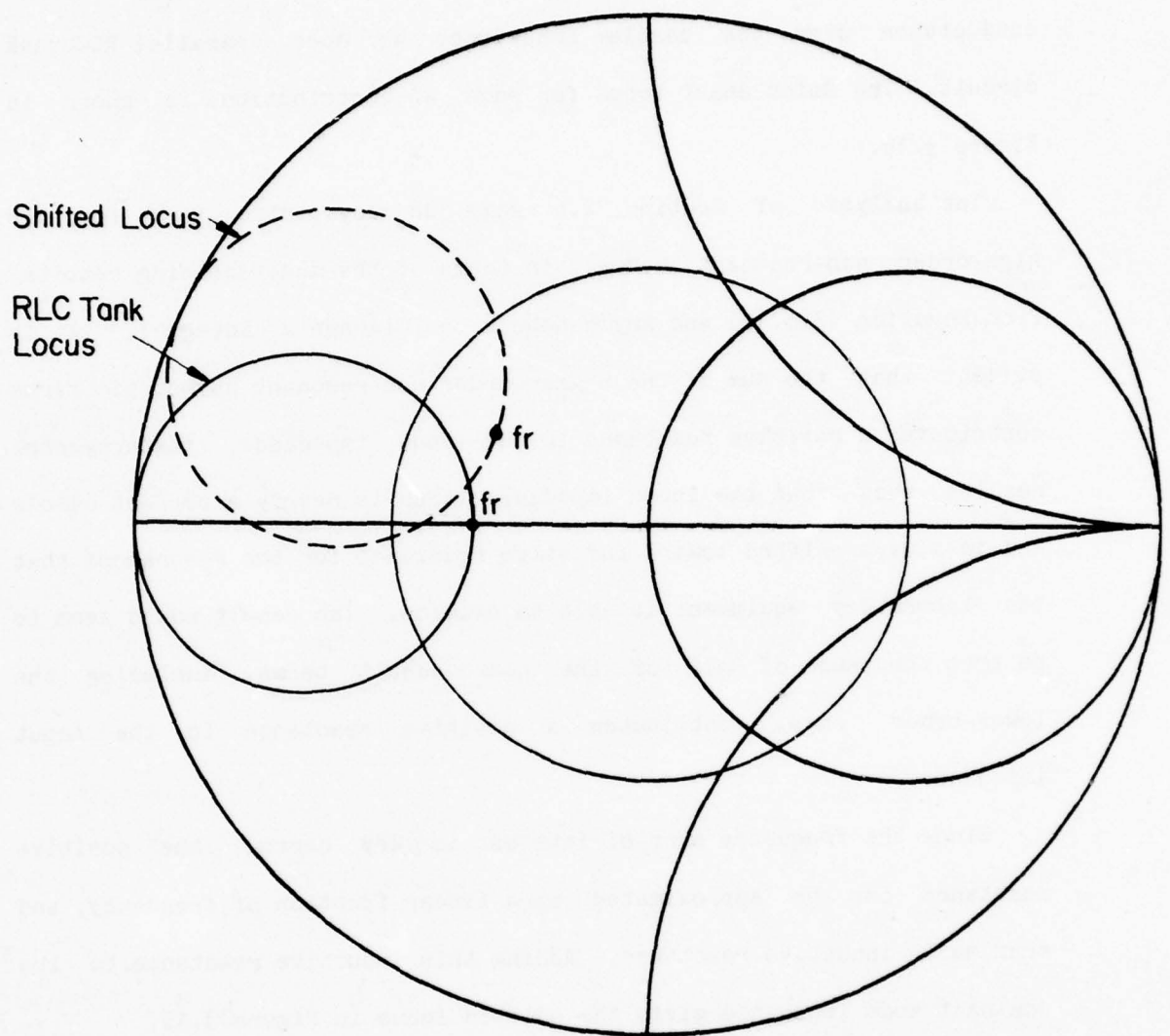for the one-port and two-port disks is shown in Figure 3.16. Equation

61

Figure 3.15. An impedance locus for an RLC tank circuit,
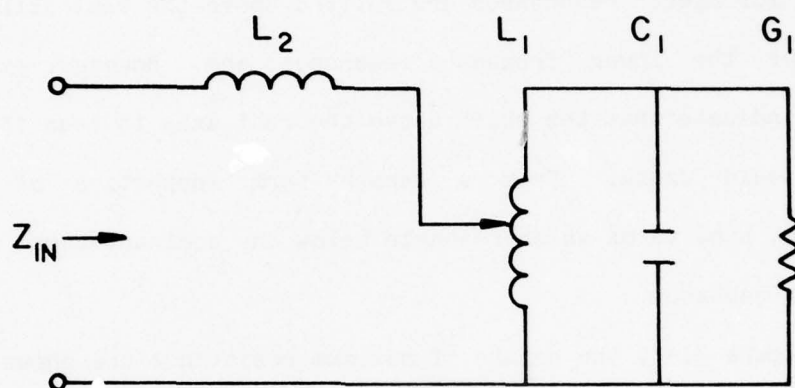and the shifted result of adding the effect
of non-resonant terms.

Figure 3.16. A simple circuit for the disk input
impedance

(2.6.4) indicates that the series inductance in Figure 3.16 is a function of the feed width and radial feed location. Since the sum of the non-resonant contributions has a factor ω, the importance of these contributions would seem to be a direct function of frequency. Indeed, the loci for higher resonances are shifted above the real axis more than those for the lower frequency resonances are. However, experimental results indicate that the shift above the real axis is less than the ω factor would cause. From a term-by-term inspection of the input impedance, some terms which resonate below the dominant term contribute negative reactance.

In Figure 3.17, the points of maximum resistance are shown for four of the radial feed locations of Section 3.2. Although the points seem to lie on a line of constant reactance, Figure 3.18 shows that the reactance increases with increasing radial feed location, as Equation (2.6.4) indicated. The results are somewhat obscured because the feed width is not actually constant when the feed is moved radially.

From this simple circuit model, "resonance" of the antenna can be defined as the point of <u>maximum input resistance</u>. This definition allows the antenna and the RLC tank of Figure 3.16 to resonate at the same frequency, since adding reactance to the RLC tank locus does not change the frequency of maximum input resistance, as seen in Figure 3.15.

3.5 Radiation Pattern Investigation

The far field radiation patterns were measured and compared to calculated results for the one-port disk antenna. The patterns for the
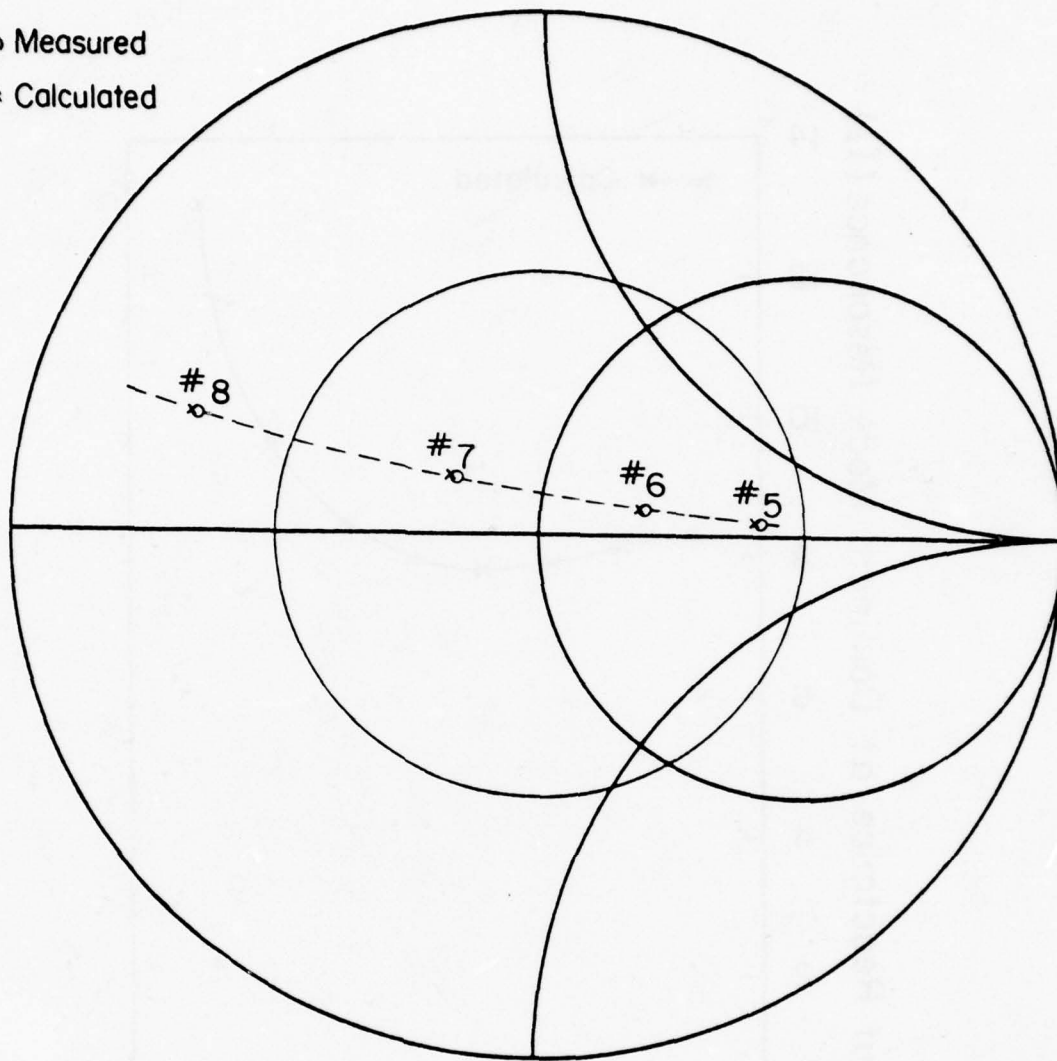
Figure 3.17. The locus of resonant input impedance points
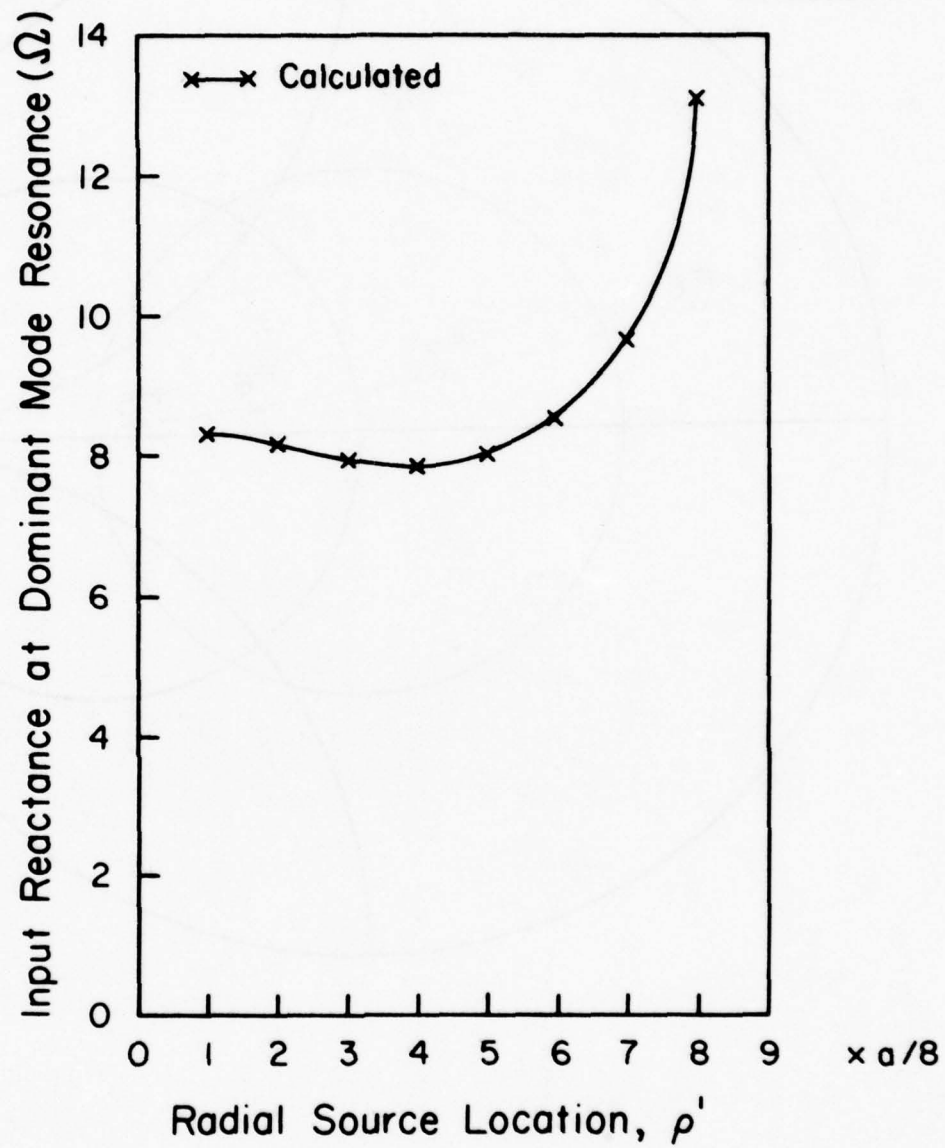for different radial feed locations.

Figure 3.18. The variation of input reactance at the
dominant mode resonance for different radial
feed locations.

multiple-port disk can also be analyzed, although they have not yet been calculated. The radiation patterns are calculated from equation (2.3.41), where the E field aperture distribution is assumed to be z directed only.

For the disk of Section 3.2, the first resonance is near 810 MHz. The calculated and measured radiation patterns are shown in Figures 3.19 to 3.24. These data indicate that the pattern bandwidth is greater than the impedance bandwidth. Qualitatively, the calculated and measured results match quite well. However, no attempt was made to take the effects of a finite ground plane into account. For frequencies near 810 MHz, the ground plane is about 12 wavelengths on a side.

For a particular mode, the radiation pattern is substantially independent of the size and resonant frequency of the disk, as long as the relative permittivity of the dielectric is held constant. With this in mind, the second mode pattern was investigated using the disk of Section 3.3. For this disk, the second resonance is near 710 MHz. The calculated and measured patterns are shown in Figures 3.25 and 3.26. Again, the agreement is seen to be quite good.

The measured results have consistently shown higher cross-polarized radiation than the theory accounts for. This might be expected since the E field at the edge of the disk is not exactly z directed, as was assumed with the simple cavity model.

Although no radiation patterns were calculated for a multiple-port disk, some were measured for the disk of Section 3.2. A shorting stud was positioned on the edge of the disk, 45 degrees from the microstrip feed. The angular reference for all two-port measurements is taken to
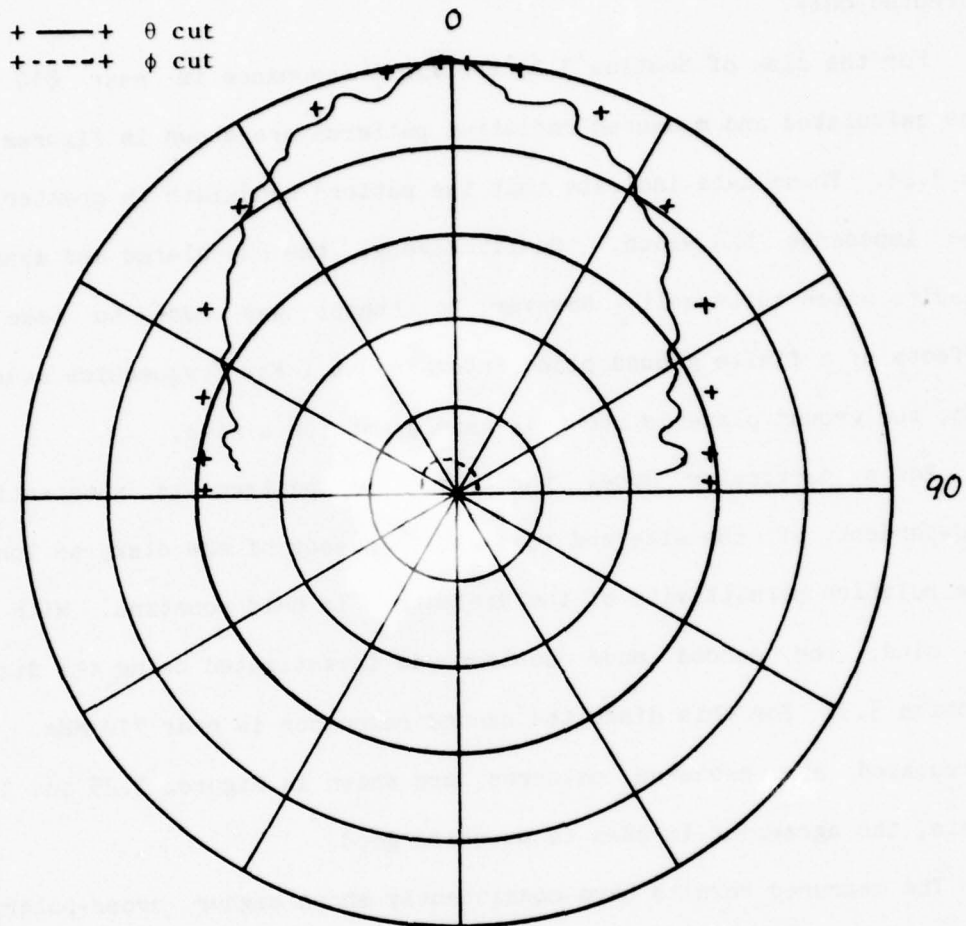
67

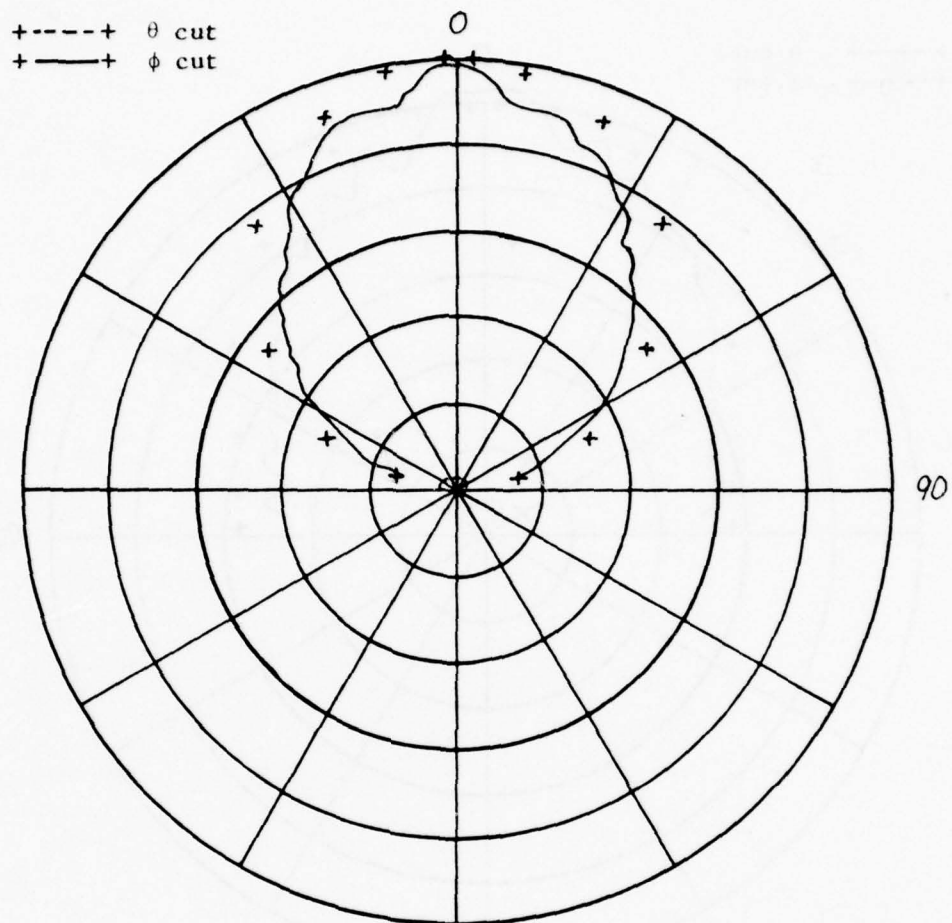Figure 3.19. First-mode radiation patterns for the 6.7 cm
disk, f = 800 MHz, φ = 0.

68

Figure 3.20.   First-mode radiation patterns for the 6.7 cm
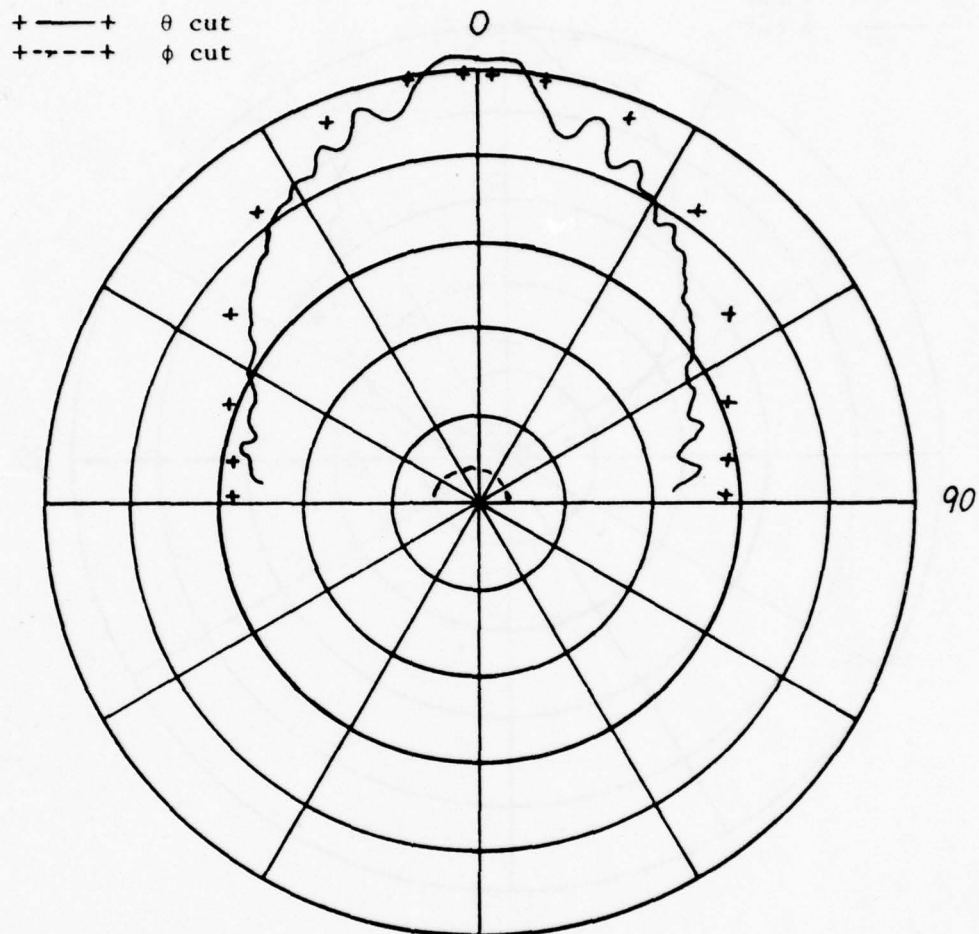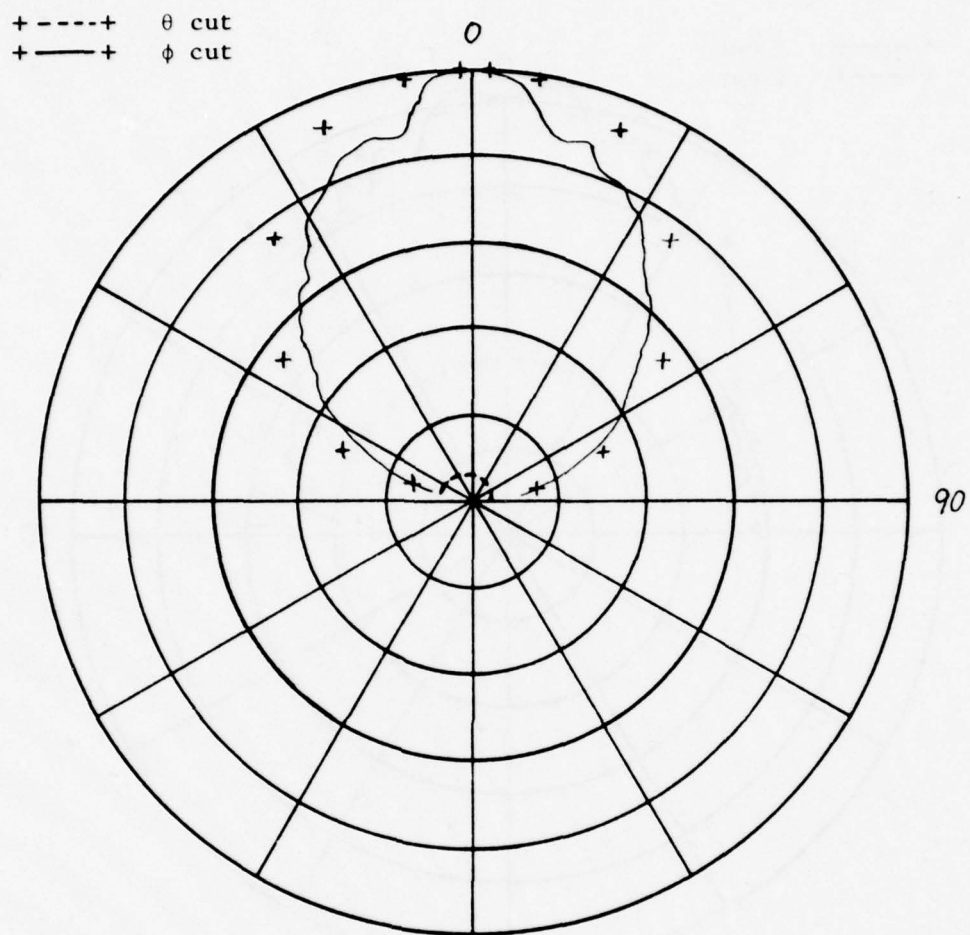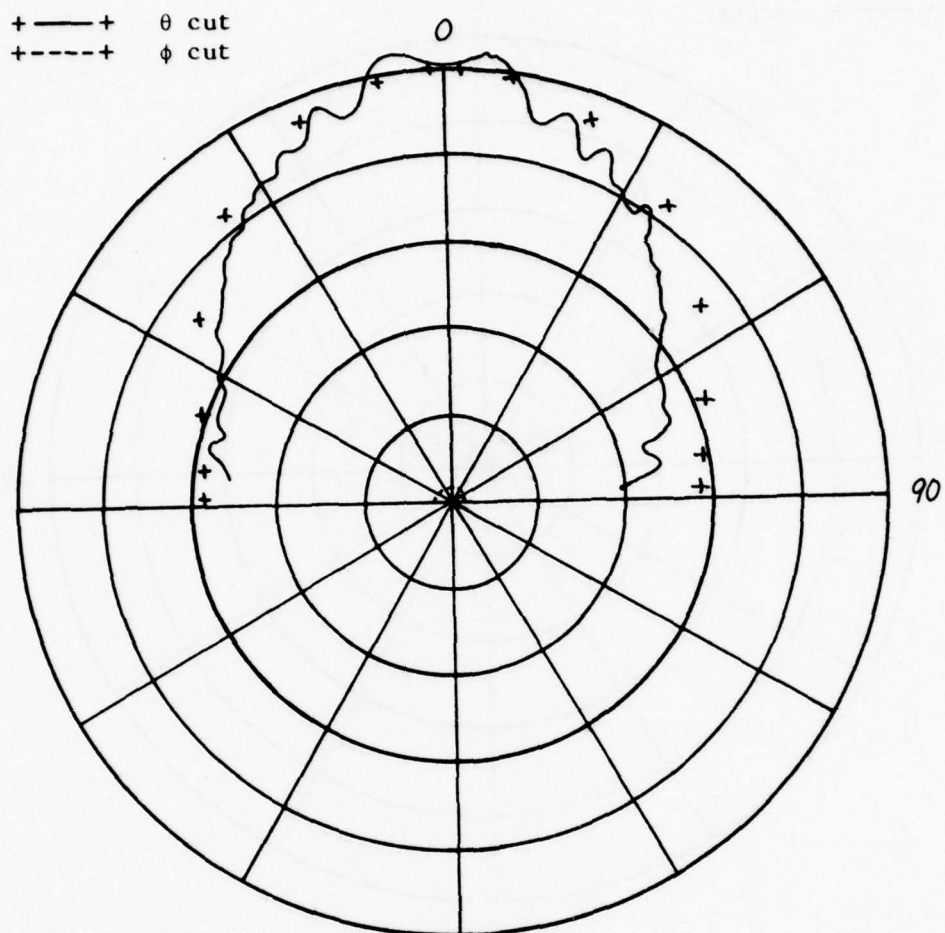disk, f = 800 MHZ, ϕ = 90.

69

Figure 3.21. First-mode radiation patterns for the 6.7 cm
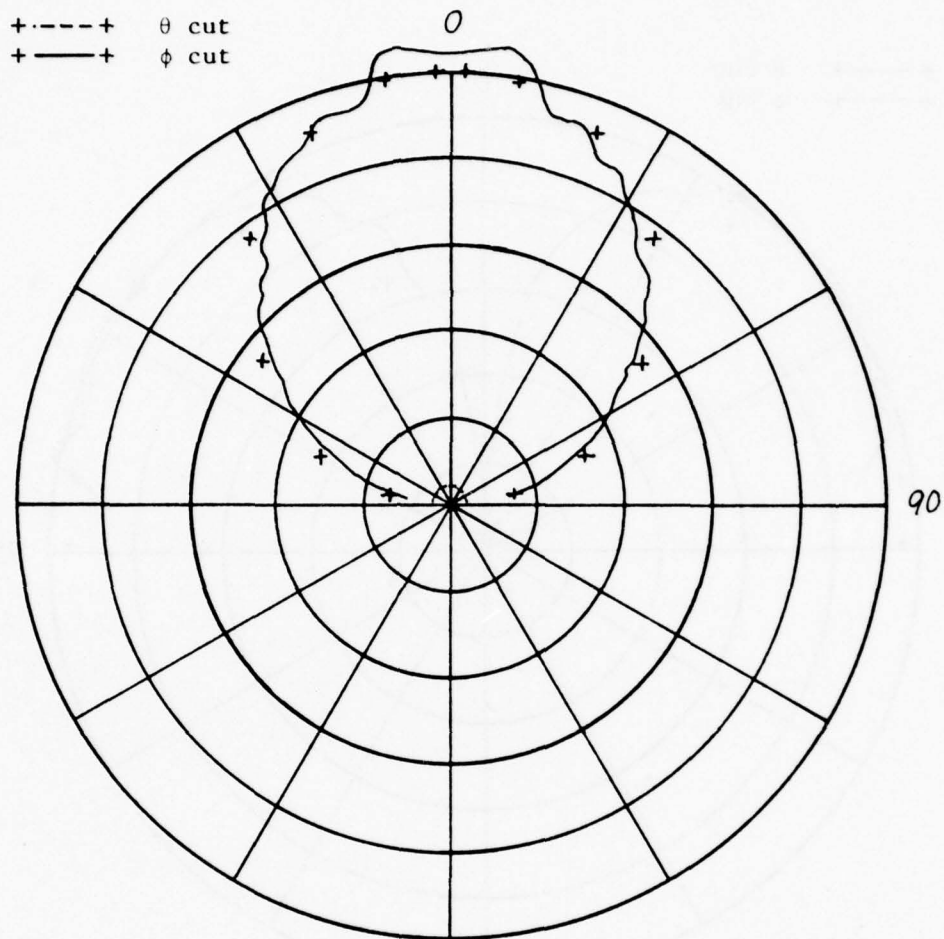disk, f = 805 MHz, ϕ = 0.

70

Figure 3.22. First-mode radiation patterns for the 6.7 cm
disk, f = 805 MHz, φ = 90.

Figure 3.23. First-mode radiation patterns for the 6.7 cm disk, f = 810 MHz, ϕ = 0.

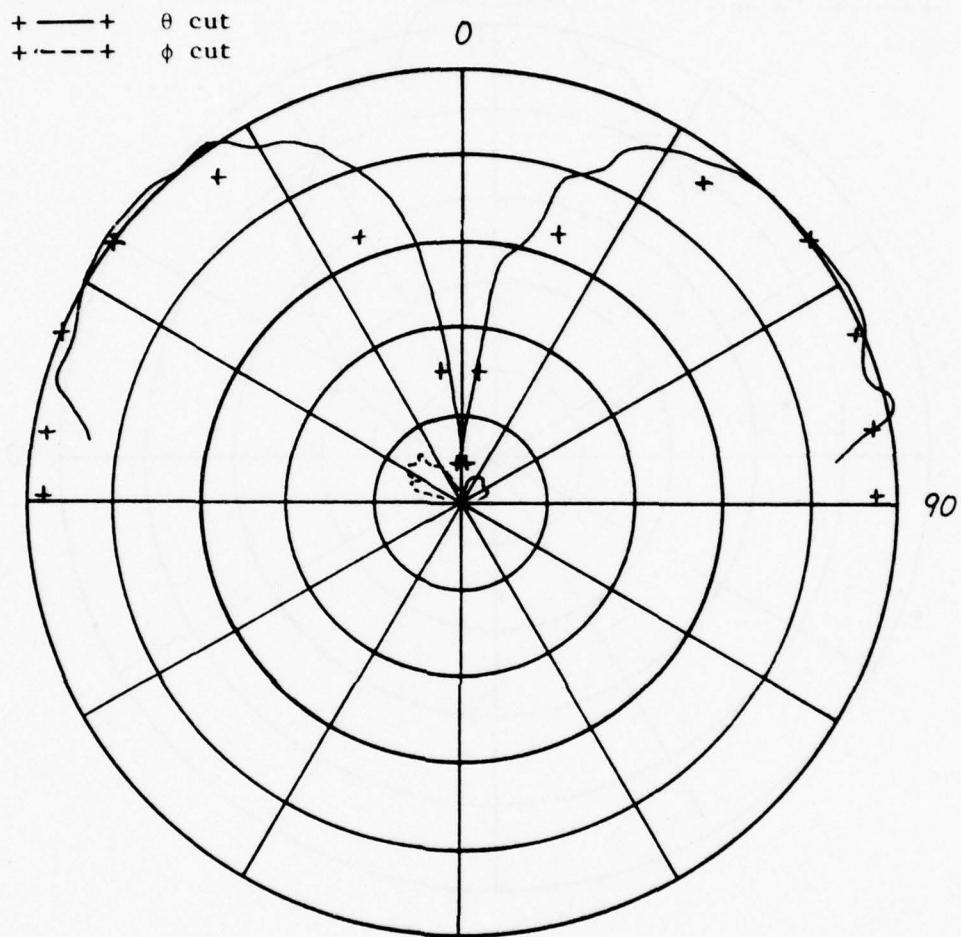Figure 3.24. First-mode radiation patterns for the 6.7 cm disk, f = 810 MHz, ϕ = 90.

73

Figure 3.25.   Second-mode radiation patterns for the
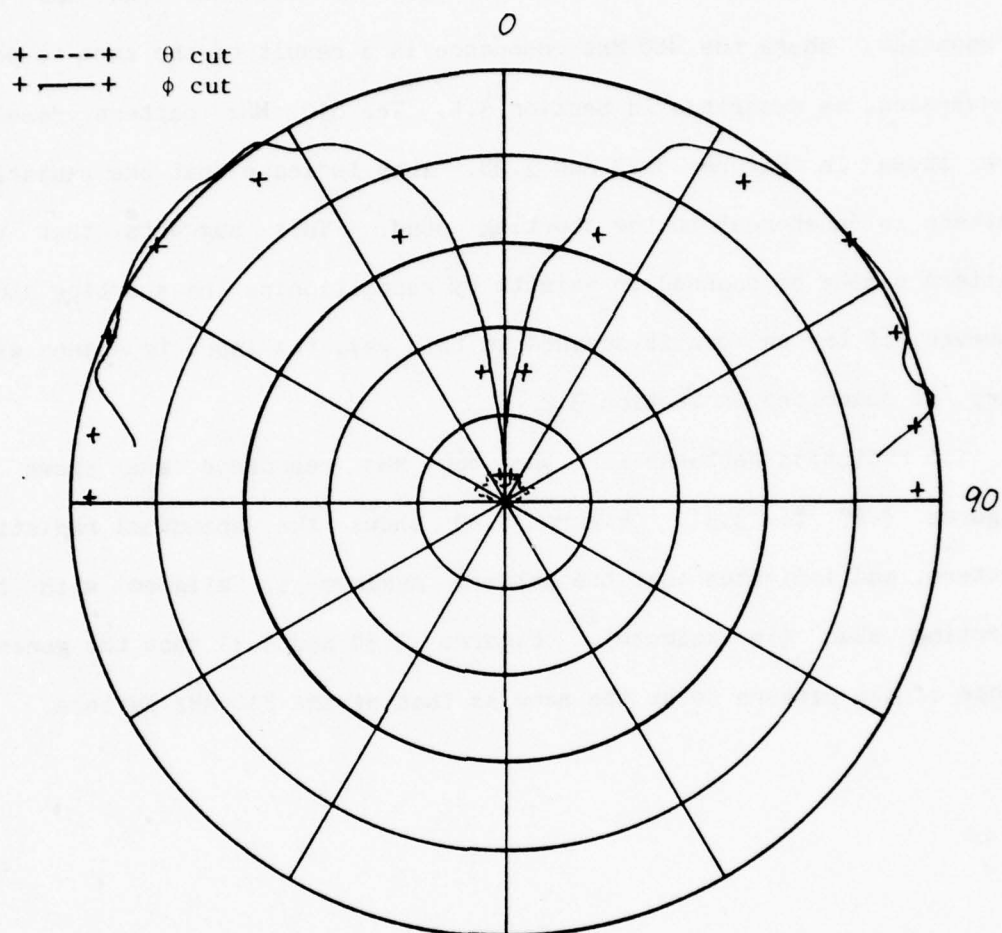12.68 cm disk, f = 710 MHz, φ = 0.

Figure 3.26.   Second-mode radiation patterns for the
12.68 cm disk, f = 710 MHz, φ = 90.

be the stud location.

The radiation pattern was measured for the 810 MHz and 860 MHz resonances, where the 860 MHz resonance is a result of the zero-to-pole conversion, as described in Section 3.4. The 810 MHz pattern results are shown in Figures 3.27 and 3.28. They indicate that the radiation pattern is "anchored" to the shorting stud. This suggests that the pattern can be be scanned in azimuth by repositioning the shorting stud. However, if the pattern is scanned in this way, the input impedance will vary, as described in Section 3.2.

The radiation patterns for the 860 MHz resonance are shown in Figures 3.29 to 3.31. Figure 3.29 shows the azimuthal radiation pattern, and indicates that the pattern maximum is aligned with the shorting stud (in azimuth). Figures 3.30 and 3.31 show the general shape of the pattern to be the same as that of the 810 MHz pattern.
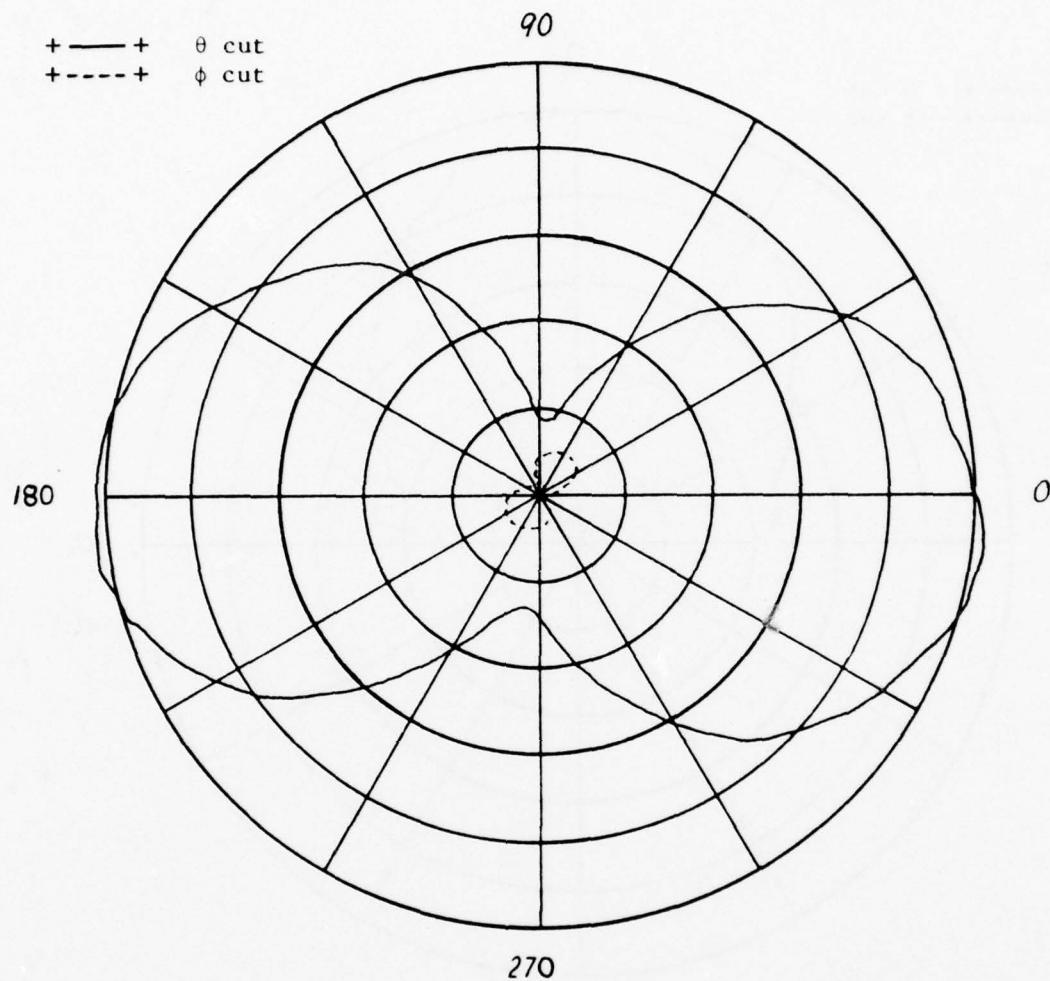
θ cut
φ cut

0

90
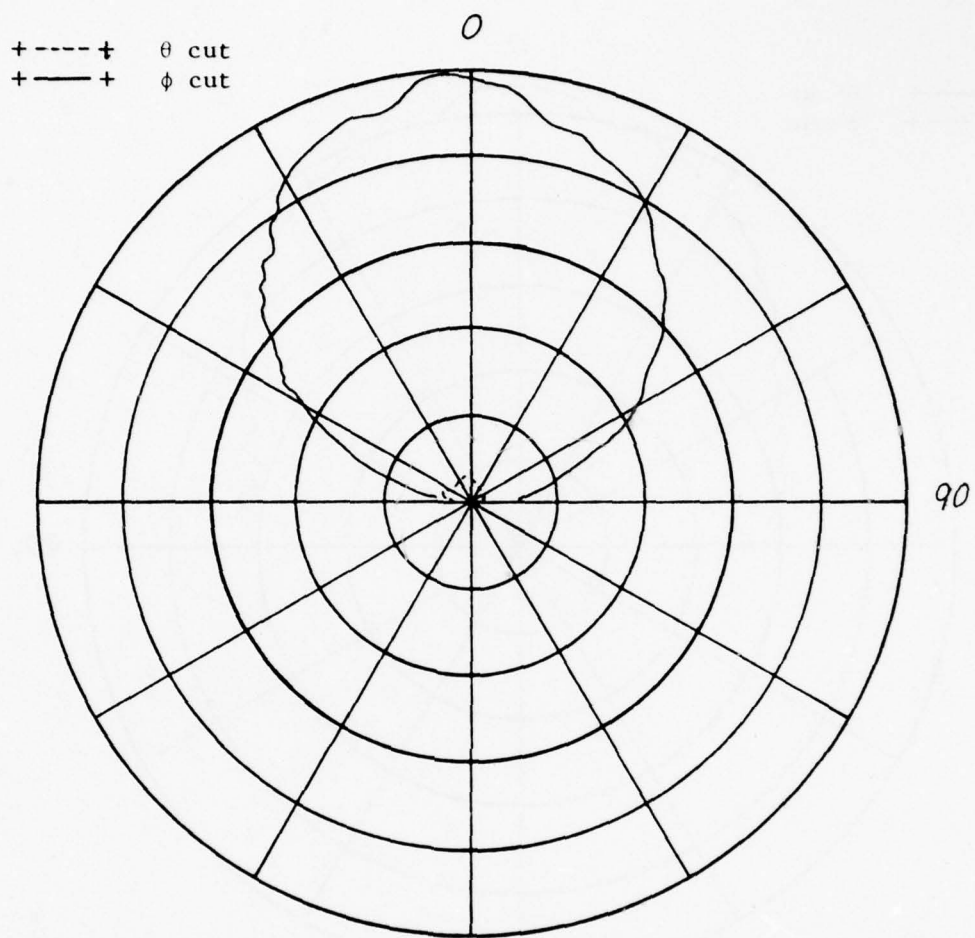
φ referenced from short.

Figure 3.27. Measured radiation patterns for the two-port
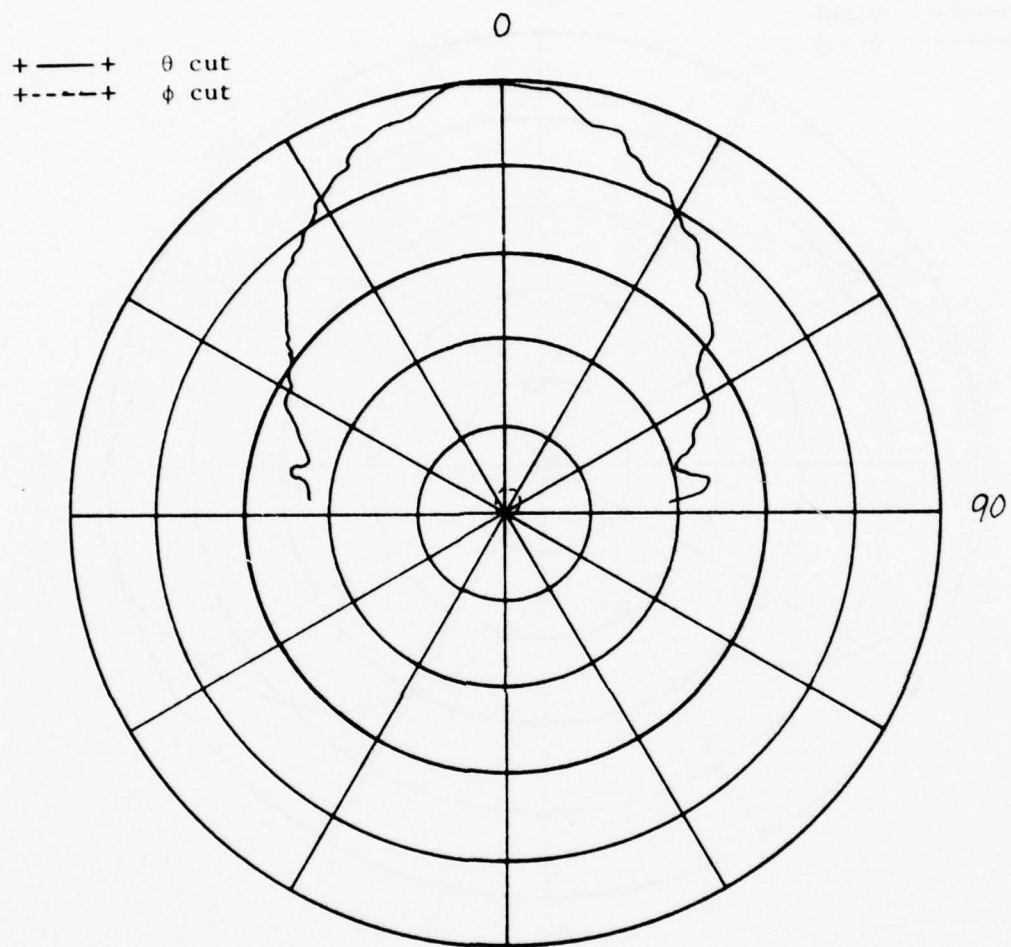6.7 cm disk, f = 810 MHz, φ = 0.
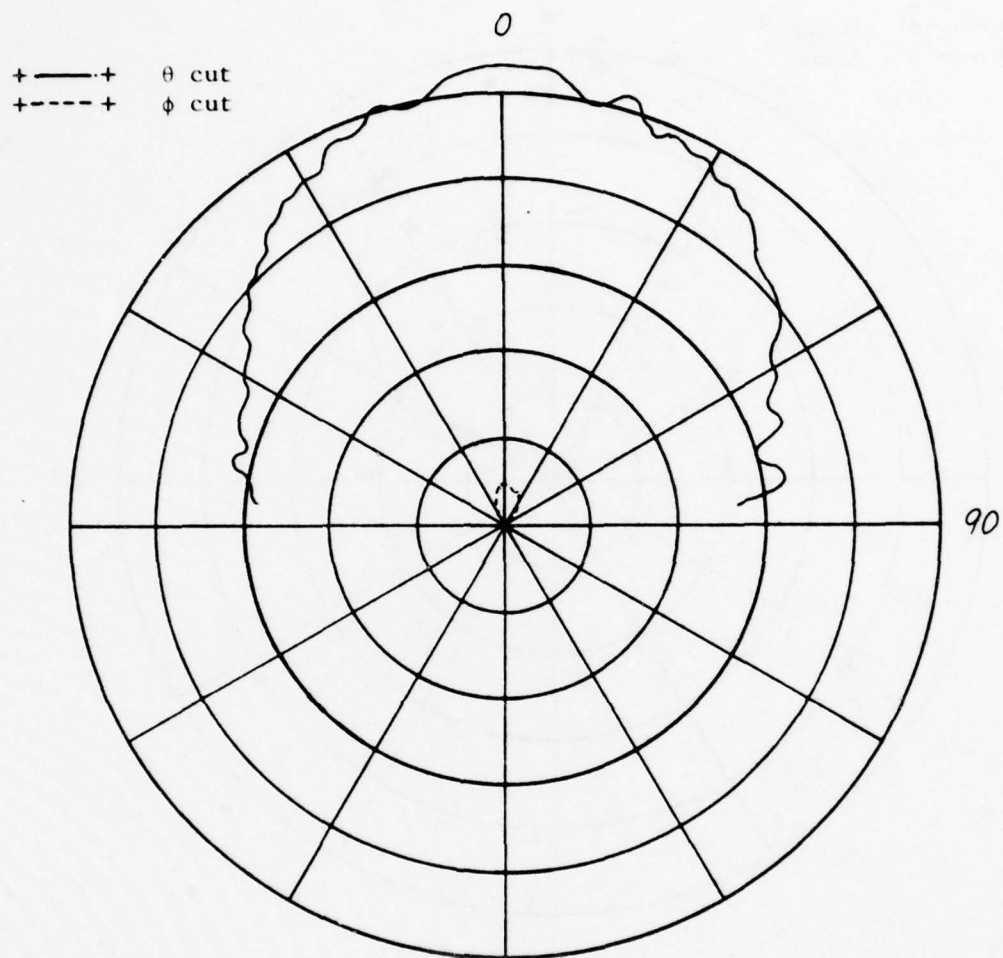
ϕ referenced from chort.

Figure 3.28. Measured radiation patterns for the two-port
6.7 cm disk, f = 810 MHz, ϕ = 90.

φ referenced from short.

Figure 3.29. Measured radiation patterns for the two-port
6.7 cm disk, f = **860** MHz, θ = 90.
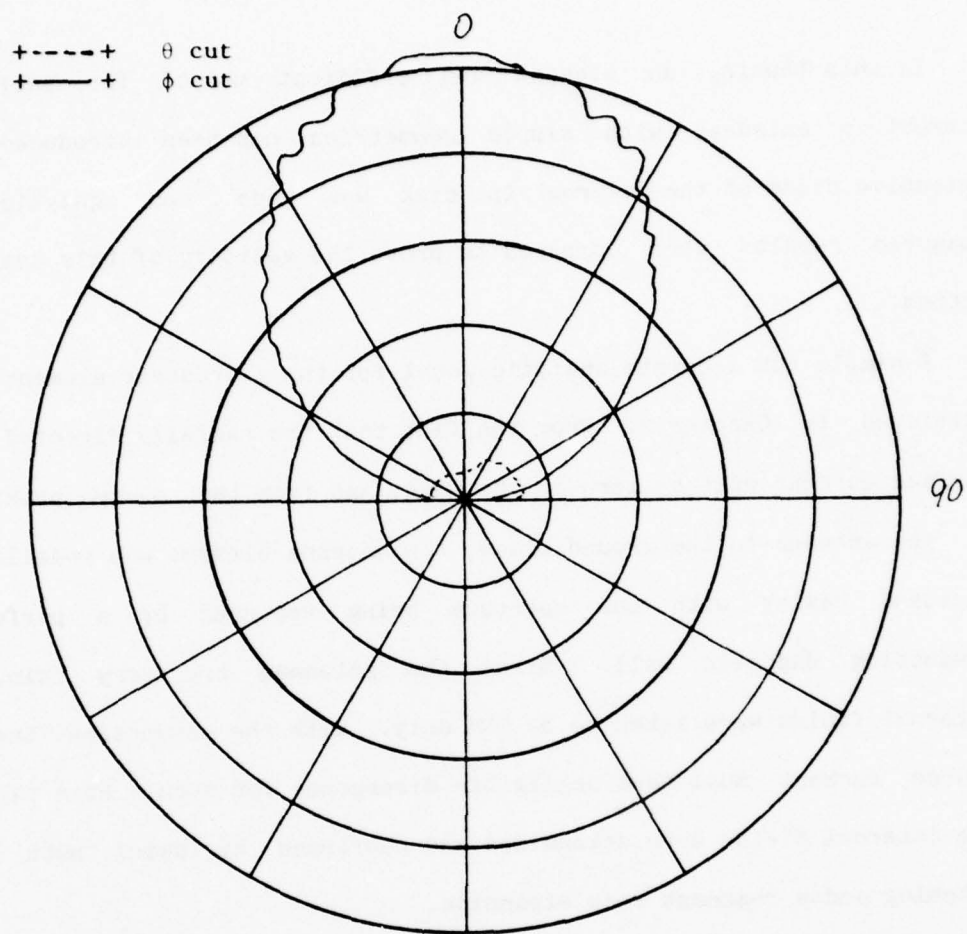
79

ϕ referenced from short.

Figure 3.30. Measured radiation patterns for the two-port
6.7 cm disk, f = **860** MHz, ϕ = 0.

Figure 3.31. Measured radiation patterns for the two-port
6.7 cm disk, f = **860** MHz, φ = 90.

CHAPTER 4

SUMMARY

In this thesis, an elegant and efficient method for analyzing microstrip antennas with simple geometries has been introduced. An extensive study of the microstrip disk was made, and analytic and measured results were compared to prove the validity of this analysis method.

A simple but accurate analytic model for the microstrip element was developed in Chapter 2. From the fact that the radially directed disk surface current must be zero at the edge, and from the close proximity of the antenna to the ground plane, the antenna element was modelled as a closed cavity with the aperture being replaced by a perfectly conducting magnetic wall. Since the antennas are very thin, the internal fields ware taken to be TEM only. With the assumption that a source current must have negligible divergence for such a thin cavity, the internal fields were determined and confirmed by using both mode matching and a resonant mode expansion.

An extremely efficient method for calculating the input impedance has been introduced in Chapter 2. The method is based upon the fact that the input impedance of a high Q system is relatively independent of the origin of any power loss. Since the microstrip antenna has a high Q, the radiated power, copper loss, and dielectric loss can be considered as a lumped dielectric loss, without substantially changing the calculated input impedance. The input impedance can then be found by finding the fields inside the perfect cavity with the modified lossy dielectric.

The microstrip disk exhibits some interesting input impedance properties, as the analysis above, and the measured data of Chapter 3 can verify. Near a resonance, the input impedance locus is an almost perfect circle, slightly shifted above the real axis of the Smith chart. Sections 2.3 and 2.6 show that the diameter of the impedance locus is a function of the dissipative losses and the radiated power, while the amount of shift above the real axis is a function of the effective width of the source current distribution.

With the simple analysis method described above, it can be shown that the disk antenna has a very useful variable input impedance property, specifically useful for matching. In Section 3.2, it is shown that by radially varying the feed location, the resonant input impedance can be varied by orders of magnitude. In Section 3.3, it is shown that a two-port disk can have the same property. By varying the angular separation of the feed point and a shorting stud, the resonant input impedance can again be varied over orders of magnitude.

Section 3.4 shows that the input impedance for the one-port disk antenna can be described very accurately and elegantly with a simple circuit model. The circuit model is shown to consist of a series inductor and a tapped RLC tank circuit, where the RLC tank represents the resonant mode contribution, and the series inductor represents the contribution of the non-resonant modes.

Both the input impedance and the radiation pattern of the disk were investigated in detail. Chapter 3 shows that the results calculated from the simple analysis are in excellent agreement with measured data. However, from the higher-order mode results, it appears that some

additional work must be done toward finding the effective source width of coaxial feeds.

The accuracy of the calculated resonant frequency of the disk was improved somewhat by using a method repeated from the literature in Appendix A. With the method, the resonant frequency error was reduced from more than 2% to less than 0.7%.

APPENDIX A

IMPROVEMENT OF CALCULATED RESONANT FREQUENCY

From the cavity model of Chapter 2, the resonant frequencies of the microstrip disk are found to be those frequencies where $(K_1 a)$ is a zero of $J_N(K_1 a)$. However, since this is a perfect cavity result, the field fringing at the edge of the disk is neglected. In reference [4] a method has been described to approximate the effects of this fringing. By finding the dc capacitance of the disk, an effective radius can be found, and is always larger than the physical radius. This larger radius is then used at the microwave frequencies for all calculations.

From the above reference,

$$a_{eff} = a \cdot Ef \tag{A.1}$$

where a_{eff} is the effective radius, and EF is the extension factor, and is defined by

$$Ef = \left\{ 1 + \frac{2t}{\pi \epsilon_r a} \left[\ln\left(\frac{\pi a}{2t}\right) + 1.7726 \right] \right\}^{1/2}. \tag{A.2}$$

The modified resonant frequency is easily calculated from

$$f \approx \frac{V_c Z_o}{2\pi a_{eff} \epsilon_r}, \tag{A.3}$$

where Z_o is a particular zero of $J_n'(Z)$, and V_c is the speed of light in free space. As an example, the modified resonant frequency is compared to the original for the disk of Figure 3.5. The measured resonant frequency is found from Figure 3.6 as 792 MHz. The unmodified resonant frequency is calculated as 810.6 MHz. This is in error by 2.3 %. From equation (A.3), the modified resonant frequency is found to be 797.7 MHz. This is error by only 0.7 %. Recall that from the definition of resonance in Section 3.4, and from Figure 3.6, the resonant frequency is independent of feed location.

APPENDIX B

GENERATION OF COMPLEX BESSEL FUNCTIONS

Numerical techniques which are used to generate complex Bessel functions are well-described in the literature. An outline is presented here for completeness.

Throughout the analysis of Chapter 2, it was seen that the wave number (K_1) was complex. Therefore, the Bessel functions having K_1 in the argument were also complex. The Bessel functions are found using the recursion relations

$$\Psi_{n-1}(z) + \Psi_{n+1}(z) = \frac{2n}{z} \Psi_n(z) \qquad \text{and}$$

$$(B.1)$$

$$\Psi_{n-1}(z) - \Psi_{n+1}(z) = 2\Psi_n'(z) \quad ,$$

where Ψ_m is either Y_m or J_m.

Since the large-order asymptotic expression for J_m approaches zero in the limit, the J_m are found by using a reverse recursion of B.1. The recursion is initiated at some high-order N, with J_{N-1} and J_N arbitrarily chosen as $(1+j0)$ and $(0+j0)$, respectively. After the recursion is completed, the requirement that

$$1 = J_o + 2 \sum_{m=1}^{\infty} J_{2m}(z) \qquad (B.2)$$

is used to denormalize all of the J_m. Since the normalization factor is

87

$$F = J_o + 2 \sum_{m=1}^{\infty} J_{2m}(z) \ , \qquad\qquad (B.3)$$

each J_m is found by dividing the respective recursion result by the normalization factor.

Once the J_m are found, the Y_m can be found using a forward recursion of B.1 since the Y_m increase with increasing order. The starting values for the recursion are

$$Y_o(z) = \frac{2}{\pi} \left[\ln\left(\frac{z}{2}\right) + \gamma \right] J_o - \frac{4}{\pi} \sum_{k=1}^{\infty} (-)^k \frac{J_{2k}(z)}{k} \ , \qquad (B.4)$$

and from the Wronskian relations,

$$Y_1(z) = \left[J_1(z) \ Y_o(z) - \frac{2}{\pi z} \right] \bigg/ J_0(z) \ . \qquad\qquad (B.5)$$

Here, the principal argument is used for $\ln(z)$ and care is taken not to specify (z) as an exact zero of $J_o(z)$, or of $J_{N-1}(z)$. Also, γ is the constant 0.5772.

To generate the J_m, an order must be chosen at which to start the recursion. The large-order asymptotic expression for J_m is

$$J_n(z) \sim \frac{1}{\sqrt{2\pi n}} \left[\frac{ez}{2n}\right]^n \qquad\qquad (B.6)$$

and as $n \to \infty$, the asymptote approaches zero. The initial choice of (0+j0) for J_N was in error by approximately

88

$$\varepsilon \doteq \frac{1}{\sqrt{2\pi n}} \left[\frac{ez}{2n}\right]^n \qquad (B.7)$$

since J_N was assumed to be zero. By specifying an acceptable absolute error ε, the starting order can be found by numerically solving the equation

$$N = \left\{ \varepsilon \left[\frac{ez}{2N}\right]^N \right\}^2 \Bigg/ 2\pi \qquad (B.8)$$

Four digit accuracy was desired, so ε was chosen as 0.0001.

89

APPENDIX C

EVALUATION OF CLAUSEN'S INTEGRAL

In Chapter 2 it became neccesary to evaluate the sums

$$f(\theta) = \sum_{k=1}^{\infty} \frac{\sin(k\theta)}{k^2} \tag{C.1}$$

and

$$g(\theta) = \sum_{k=1}^{\infty} \frac{\cos(k\theta)}{k^3} . \tag{C.2}$$

Equation C.1 is a restatement of Clausen's integral, found in any major handbook, and is just

$$f(\theta) = \theta \left[1 - \ln(\theta) + 2 \sum_{k=1}^{\infty} \frac{\zeta(2k)}{2k(2k+1)} \left(\frac{\theta}{2\pi}\right)^{2k} \right] , \tag{C.3}$$

where ζ is the Rieman-Zeta function, also found in most handbooks. Although neither C.1 nor C.3 is a closed-form expression, C.3 converges much more rapidly then does C.1.

Equation C.2 is related to C.1 since

$$\sum_{k=1}^{\infty} \frac{\cos(k\theta)}{k^3} = - \int_{0}^{\infty} \sum_{k=1}^{\infty} \frac{\sin(k\theta)}{k^2} d\theta + \zeta(3) . \tag{C.4}$$

Thus C.2 can be restated as

90

$$g(\theta) = \theta^2 \left[\frac{\ln(\theta)}{2} - \frac{3}{4} + 2 \sum_{k=1}^{\infty} \frac{\zeta(2k)}{2k(2k+1)(2k+2)} \left(\frac{\theta}{2\pi}\right)^{2k} \right], \quad \text{(C.5)}$$

which has a much more rapid rate of convergence than C.2.

1·0   2·8   2·5

3·15   2·2

1·1   3·5   2·0

4·0

4·5   1·8

1·25   1·4   1·6
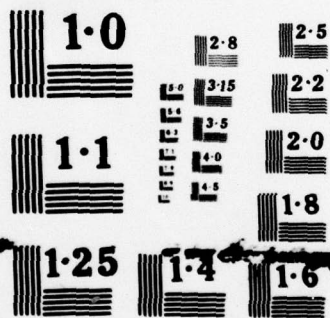
NATIONAL BUREAU OF STANDARDS
MICROCOPY RESOLUTION TEST CHART

LIST OF REFERENCES

[1] R. E. Munson, "Conformal Microstrip Antennas and Microstrip Arrays", IEEE Transactions of Antennas and Propagation, vol. AP-22, no. 1, pp. 74-78, January 1974

[2] A. G. Derneryd, "Mutual Coupling in Array Antennas", School of Elect. Eng., Chalmers University of Technology, Goteborg, Sweden, Tech. Report No. 60, February 1976

[3] P. K. Agrawal and M. C. Bailey, "An Analysis Technique for Microstrip Antennas", IEEE Transactions of Antennas and Propagation, vol. AP-25, pp. 756-759, November 1977

[4] L. C. Shen, "Resonant Frequency of a Circular Disk, Printed Circuit Antenna", IEEE Transactions of Antennas and Propagation, vol. AP-25, pp. 595-596, July 1977

[5] Y. T. Lo, D. Solomon, F. Ore, D. D. Harrison, "Study of Microstrip Antennas, Microstrip Phased Arrays, and Microstrip Feed Networks", Report No. RADC-TR-77-406, October 21, 1977 (A053005)

MISSION
of
Rome Air Development Center

RADC plans and executes research, development, test and selected acquisition programs in support of Command, Control Communications and Intelligence (C^3I) activities. Technical and engineering support within areas of technical competence is provided to ESD Program Offices (POs) and other ESD elements. The principal technical mission areas are communications, electromagnetic guidance and control, surveillance of ground and aerospace objects, intelligence data collection and handling, information system technology, ionospheric propagation, solid state sciences, microwave physics and electronic reliability, maintainability and compatibility.